ADP-ribose triggers neuronal ferroptosis by rewiring purine and pyrimidine metabolism

Haoqi Ni[1,2,7], Yingying He[1,3,7], Peng Cui[1,7], Hebing Chen[4,7], Guoqing Lv[1,3], Huiyan Lei[5], Feng Wang[1], Qichuan ZhuGe[2], Baodong Chen[1], Ling Liang[6], Yong Zhang[6], Fuping You[6] and Lin Yuan[1,7*]

[1]Institute of Biomedical Sciences, Peking University Shenzhen Hospital, Shenzhen 518036, China;

[2]Zhejiang Key Laboratory of Aging and Neurological Disorder Research, the First Affiliated Hospital of Wenzhou Medical University, Wenzhou, 325000, China;

[3]Department of Biochemistry, University of Texas Southwestern Medical Center, Dallas, TX, 75390, USA;

[4] Institute of Health Service and Transfusion Medicine, Beijing 100850, China;

[5]Department of Physiology, University of Texas Southwestern Medical Center, Dallas, TX, 75390, USA;

[6]School of Basic Medical Sciences, Peking University Health Science Center, Beijing 100191, China;

[7]These authors contributed equally to this work.

*Corresponding author. Email: yuan_lin@bjmu.edu.cn

Running title: ADP-ribose induces neuronal ferroptosis

ABSTRACT

Hyperactivation of NAD^+-consuming pathways frequently occurs in neurological diseases, however therapies replenishing NAD^+ levels show limited therapeutic efficacy, indicating more complex underlying pathophysiology. Here, we delineate a pathogenic link between ADP-ribose —a product of NAD^+ consumption—and a metabolic rewiring-dependent form of neuronal ferroptosis. We demonstrate that oxidative stress induces neurons to produce ADP-ribose through the PARP1-PARG axis. ADP-ribose directly binds and inhibits the equilibrative nucleoside transporter ENT2, remodeling *de novo* purine and pyrimidine synthesis by hyperactivating the inosine-hypoxanthine-xanthine oxidase and glutamine-dihydroorotate-dihydroorotate dehydrogenase axes. This overproduces superoxide radicals and drives lipid peroxidation and neuronal ferroptosis. Elevated ADP-ribose levels were observed in neurological disease models, and acute ADP-ribose exposure severely reduced mouse brain neurons *in vivo*. Critically, interventions blocking ADP-ribose signaling alleviated cognitive decline in mouse intracerebral hemorrhage models. Our findings characterize ADP-ribose signaling as linking NAD^+ consumption to neuronal ferroptosis, and provide a theraputic strategy for neuropathologies involving NAD^+ consumption and oxidative stress.

KEYWORDS: ferroptosis, ADP-ribose, NAD, ENT2, XO, DHODH, neurological diseases

INTRODUCTION

Maintenance of nicotinamide adenine dinucleotide (NAD^+) homeostasis through its intracellular physiological level between 0.2 and 0.5 mM is essential for neuronal redox and bioenergetic homeostasis [1]. However, hyperactivation of the major NAD^+-consuming enzyme families—poly(ADP-ribose) polymerases (PARPs), Sirtuins, and NAD nucleosidases (*e.g.*, CD38, CD157, and SARM1)—is associated with several neurological disorders, including Alzheimer's disease (AD) and hemorrhagic stroke [1,2]. These NAD^+-consuming enzyme families ultimately consume NAD^+ to yield ADP-ribose and release nicotinamide [3]. While supplementation of NAD^+ or its precursors shows limited therapeutic benefit in patients with hyperactivated NAD^+-consuming enzymes [3], indicating more complex underlying pathological mechanism.

Under oxidative stress conditions, increases in activity of PARP1 lead to upregulation of NAD^+ consumption and protein poly-ADP-ribosylation [4]. Poly-ADP-ribosylation is reversible and can be degraded by poly(ADP-ribose) glycohydrolase (PARG) into ADP-ribose polymers ("PAR") and ADP-ribose monomers ("ADP-ribose") [5]. PAR can induce mitochondrial apoptosis-inducing factor (AIF) release and nuclear translocation, leading to "parthanatos" cell death [6]. However, PAR is rapidly degraded by PARG into ADP-ribose [5]. The function of ADP-ribose remains unclear, although some studies show PARG knockout mice exhibit higher brain damage after stroke[7], whereas others report PARG inhibitors can rescue neuronal cell death induced by the glutamate receptor agonist NMDA[8]. Collectively, these findings suggest that both PAR and ADP-ribose accumulation may influence neuronal cell death.

Ferroptosis is a regulated form of cell death that depends on iron and Lands' cycle, characterized by excessive lipid peroxidation[9]. Lipid peroxidation is initiated by the formation of a carbon-centered radical on polyunsaturated fatty acyl phospholipids (PUFA-PLs), which can be seed by

71 hydroxyl or peroxyl radicals generated from iron-catalyzed Fenton reactions [10]. If not converted
72 to a lipid hydroperoxide and subsequently reduced to the corresponding alcohol, the propagation
73 of free-radical-mediated reactions will commence, ultimately resulting in a myriad of secondary
74 products, disruption of membrane integrity, and membrane rupture with the release of cellular
75 contents [11]. Due to their high PUFA-PL content, neuronal menbranes are particularly susceptible
76 to peroxidation [11]. While cells have evolved multiple defenses against ferroptosis by increasing
77 antioxidant capacity, mainly via the glutathione peroxidase 4 (GPX4)/glutathione (GSH)
78 system[12-14], the ferroptosis suppressor protein 1 (FSP1)/coenzyme Q (CoQ) system[15,16], and the
79 GTP cyclohydrolase-1 (GCH1)/tetrahydrobiopterin system[17], intracellular metabolic
80 dysregulation causing redox imbalance appears to be the essential trigger of lipid hydroperoxide
81 and ferroptosis.

82 Here, we found that exposure to ferroptosis inducers promoted the accumulation and release of
83 ADP-ribose from cultured primary neurons. Using thermal proteome analysis (TPP) and mass
84 spectrometry-based metabolomics, we show that extracellular ADP-ribose directly binds to the
85 equilibrative nucleoside transporter 2 (ENT2) protein, inhibiting its bidirectional transport of
86 purine and pyrimidine nucleosides. This transport inhibition led to overactivation of the inosine-
87 hypoxanthine-xanthine oxidase (XO) and glutamine-dihydroorotate-dihydroorotate
88 dehydrogenase (DHODH) axes in neurons, resulting in excessive superoxide anion production
89 and lipid peroxidation-dependent ferroptotic death of neurons. Microinjecting ADP-ribose into
90 mouse brains dramatically reduced neuron numbers, an effect rescued by co-administering
91 XO/DHODH inhibitors. Furthermore, intracerebral hemorrhage (ICH) induced production in
92 mouse neurons *in vivo* with subsequent cognitive decline, aspects mitigated by attenuating ADP-

93 ribose production via PARP1 knockdown or microinjecting the ADP-ribose pyrophosphatase
94 Nudix hydrolase 9 (NUDT9).

95 **RESULTS**

96 **Ferroptotic metabolite ADP-ribose induces neuronal cell death and is elevated in**
97 **neurological disease models**

98 Given that apoptotic cells release metabolites that can impact neighboring tissues [18,19], we
99 investigated whether metabolites released from ferroptotic neurons affect unstressed neurons.
100 Primary cortical neurons isolated from E16.5 mice (Fig. S1A) were cultured *in vitro* for 2 weeks
101 to mature and then exposed for 6 hours to 100 μM hemin[20,21], a ferroptosis inducer that model
102 intracerebral hemorrhage *in vitro* (Fig. 1A). The medium was subsequently replaced with fresh
103 medium and incubated for an additional 6 hours, at which point a CCK-8 assay showed ~70%
104 cell death (Fig. S1B). When this conditioned medium was collected and concentrated ten-fold,
105 despite the absence of detectable hemin, it induced cell death upon addition to mature primary
106 cortical neuron cultures (Fig. 1B). This observation suggests ferroptotic neurons release
107 extracellular factor(s) inducing death in unstressed neurons. To determine if the released factor(s)
108 was proteinaceous, we heat-treated the conditioned medium at 95°C for 5 minutes before adding
109 to mature primary cortical neuron cultures, which did not prevent cell death (Fig. 1, A and B).
110 Fractionation by molecular sieve indicated the factor(s) were <1 kDa (Fig. 1, A and B).
111 Untargeted metabolomics identified ADP-ribose as the small molecule most upregulated (> 90-
112 fold) in the medium after hemin exposure (Fig. S1C and Supplementary Table 1). MS-based
113 quantification using an authentic standard curve confirmed significantly higher intracellular and
114 extracellular ADP-ribose in hemin-treated neurons (Fig. 1, C and D and Fig. S1D).

115 We next tested if ADP-ribose directly induce neuronal cell death. ADP-ribose exposure killed
116 murine naïve primary cortical neurons (24h post-plating), mature primary cortical neurons (2
117 weeks post-plating), murine hippocampal HT22 neurons, and human SH-SY5Y neuroblastoma
118 cells (Fig. 1, E and F and Fig. S1, E and F), with slight differences in sensitivity. In contrast,
119 ADP-ribose exposure did not kill murine primary astrocytes (Fig. S1G). Furthermore, neither
120 ADP-ribose precursors (PAR) nor its degradation products (AMP and R5P) induced neuronal
121 death (Fig. 1G and S1H). Moreover, cell death was not observed when the conditioned medium
122 was treated with ADP-ribose pyrophosphatase NUDT9 prior to assays, corroborating ADP-
123 ribose specificity (Fig. S2, A to D). Additionally, ADP-ribose sensitized primary cortical neurons
124 to hemin- and L-homocysteic acid-induced cell death (Fig. S2E). Collectively, these data
125 indicate ADP-ribose exposure triggers neuronal cell death.

126 We subsequently explored the potential *in vivo* relevance of stress-induced ADP-ribose
127 production in neurons in multiple neurological disease models. LC-MS/MS quantification of
128 brains from the well-characterized TauR406W *Drosophila melanogaster* model, which displays
129 early-onset familial dementia features [22], showed elevated ADP-ribose levels versus wild-type
130 flies (Fig. 1H). Furthermore, we examined brain cells from Alzheimer's disease (AD) mouse
131 models, specifically APP/PS1 and 5×FAD mice [23,24]. While hippocampal neuronal ADP-ribose
132 gradually increased with age in wild-type mice, it increased substantially more in APP/PS1 and
133 5×FAD mice (Fig. 1I). Compared to age-matched wild-type littermates, both transgenic lines
134 exhibited significantly higher ADP-ribose levels in cerebral cortical and hippocampal neurons
135 (Fig. 1, J and K). Additionally, cerebrospinal fluid (CSF) samples from AD and control subjects
136 showed elevated median ADP-ribose in AD patients (n=207, 2.53 μg/ml) versus controls (n=196,

137 0.03 μg/ml, $P<0.0001$) (Fig. 1L). Hence, the presence of elevated brain ADP-ribose in
138 neurological disease models implicates the potential pathological relevance of ADP-ribose.

139 **ADP-ribose production is induced by the PARP1-PARG axis**

140 We investigated how ADP-ribose is generated in ferroptotic neurons. Exposure of neurons to
141 hemin reduced GSH levels and induced H_2O_2 generation (Fig. S3A). Under oxidative stress,
142 PARP1 is activated and utilizes NAD^+ as a substrate to catalyze protein poly-ADP-ribosylation,
143 which is rapidly degraded by PARG to yield ADP-ribose, contributing to the intracellular ADP-
144 ribose pool [8,25-27]. We found that primary cortical neurons from *Parp1* neuron-specific knockout
145 mice exhibited reduced NAD^+ consumption and ADP-ribose production upon hemin exposure
146 compared to wild-type controls (Fig. 2, A and B; fig. S3B). Moreover, under cysteine withdrawal,
147 ADP-ribose production was significantly reduced in PARP1 knockout neurons compared to
148 wild-type (Fig. 2C). To confirm PARP1's role in production of ADP-ribose precursors, we
149 pretreated neurons with the PARG inhibitor PDD to block rapid poly-ADP-ribosylation
150 hydrolysis. We observed that exposure to hemin, erastin and glutamate significantly increased
151 poly-ADP-ribosylation (Fig. 2D and fig. S3C), which was reduced by the radical scavenger α-
152 TOC (Fig. S3C). Additionally, the PARP1 degrader iRucaparib-AP6[28] diminished hemin-,
153 erastin- and glutamate-induced poly-ADP-ribosylation (Fig. 2D; fig. S3, D to F). These results
154 indicate that activated PARP1 promotes ADP-ribose production under ferroptosis-induced
155 oxidative stress.

156 We further tested whether inhibition of the PARP1-PARG axis could prevent hemin-induced
157 ADP-ribose generation. Specifically, murine primary cortical neurons were pre-treated with PDD
158 or iRucaparib-AP6 for 1 hour followed by 6 hours of exposure to 100 μM hemin and a further 6
159 hours of culture in hemin-free medium (Fig. S3G). Although significant cell death was still

160 detected by CCK-8 assay (Fig. S3H), no ADP-ribose was detected in the conditioned medium
161 and no additional cell death was observed upon treating murine primary neuron cultures with this
162 conditioned medium (Fig. 2, E and F). These results suggest that ferroptosis-stressed neurons
163 generate ADP-ribose through the PARP1-PARG axis, with subsequent ADP-ribose release due
164 to membrane integrity disruption.

165 **ADP-ribose targets and inhibits the nucleoside transporter ENT2**

166 To uncover potential intracellular targets of ADP-ribose, we employed thermal proteome
167 profiling (TPP), which can unbiasedly identify ligand-protein interactions based on increased
168 protein thermal stability upon complex formation[29]. Notably, intracellular ADP-ribose levels did
169 not increase in SH-SY5Y cells after exposure to semi-lethal doses (Fig. S3I), suggesting ADP-
170 ribose binds plasma membrane proteins to trigger cell death. Therefore, we treated total SH-
171 SY5Y proteins with ADP-ribose and performed TPP, which identified a total of 7,263 proteins.
172 Among the top 5-ranking candidates with >2-fold thermal stability increases upon ADP-ribose
173 treatment, the equilibrative nucleoside transporter 2 (ENT2), also known as SLC29A2, stood out
174 prominently as a plasma membrane protein (Fig. 2G and Supplementary Table 2). Furthermore,
175 we validated these results by treating murine primary neurons with varying doses of ADP-ribose
176 and detecting a dose-dependent increase in ENT2 thermal stabilization (Fig. 2H). In addition,
177 direct ADP-ribose binding to *E. coli*-purified ENT2 was observed via microscale thermophoresis
178 and thermal melting assays (Fig. S4, A and B). However, no ENT2 binding was detected to
179 either PAR or di-ADP-ribose in thermal melting assays, implicating ADP-ribose specifically (Fig.
180 S4C).

181 ENT bidirectionally transports various purine and pyrimidine nucleosides, including uridine,
182 cytidine, inosine and hypoxanthine [30-32]. Using the ENT1 crystal structure (PDB:6OB6)[33] and an

183 AlphaFold2 model, we performed *in silico* docking suggesting that ADP-ribose occupies the
184 ENT2 nucleoside transport pocket (Fig. S4, D to F). ^{13}C-metabolic flux analysis demonstrated
185 that ADP-ribose pretreatment abolished uptake of substrates like uridine and inosine into SH-
186 SY5Y cells without inducing cell death (Fig. 2I, Fig. S4G and Supplementary Table 3). High-
187 dose nitrobenzylthioinosine (NBMPR, 100 μM), an ENTs inhibitor, also inhibited substrate
188 uptake (Fig. S4H). Export of substrates from SH-SY5Y cells was also abolished upon ADP-
189 ribose pretreatment (Fig. S4, I and J). Metabolomics revealed that ADP-ribose exposure reduced
190 intracellular uridine and cytidine, while increasing inosine and hypoxanthine levels (Fig. S4, K
191 and L). Thus, extracellular ADP-ribose inhibits ENT2-mediated transport of pyrimidine and
192 purine nucleosides.

193 Mutations in ENT2 residues Q76/Q145 attenuated ADP-ribose binding *in vitro* (Fig. 2J), and
194 abolished substrate transport impairment by ADP-ribose in HT22 cells (Fig. 2K, and Fig. S5A).
195 HT22 cells expressing mutant ENT2 were resistant to ADP-ribose-induced death versus wild-
196 type cells (Fig. 2L). The ENT2 inhibitors dipyridamole and high-dose NBMPR partially reduced
197 primary neuron viability, implicating ENT2 inhibition induces neuronal death (Fig. S5B). ENT2,
198 but not ENT1, knockdown sensitized SH-SY5Y cells to ADP-ribose-induced cell death (Fig. 2M
199 and Fig. S5, C to G). Retinoic acid (RA)-differentiated SH-SY5Y cells[34], which downregulate
200 ENT2 (Fig. S5, H and I), exhibited heightened sensitivity to ADP-ribose-induced death versus
201 undifferentiated cells (Fig. 2N). Stably expressing ENT2, but not ENT1/3, rendered
202 differentiated cell resistance to ADP-ribose (Fig. 2N, and Fig. S5J). Collectively, these results
203 indicate that ADP-ribose triggers neuronal cell death by inhibiting ENT2.

204 **ADP-ribose is a neuronal ferroptosis inducer**

205 We further characterized the cell death pathway(s) induced by ADP-ribose in neurons using
206 inhibitors of distinct cell death forms. ADP-ribose-mediated cell death was fully rescued by
207 ferroptosis inhibitors including the iron chelator deferoxamine (DFO) and the radical-trapping
208 antioxidants—α-Tocopherol (α-Toc), ferrostatin-1 (Fer-1) and liproxstatin-1 (Lip-1) (Fig. 3A
209 and Fig. S6, A and B). Inhibitors of autophagy or apoptosis did not exert protective effects (Fig.
210 3A and Fig. S6, A and B). Additionally, ADP-ribose treatment increased levels of the lipid
211 peroxidation marker 4-HNE in murine primary cortical neurons (Fig. 3B). Cell death induced by
212 ENT2 knockdown or inhibition with NBMPR was also rescued by Fer-1 or Lip-1 (Fig. 3C and
213 S6C). Together, these results demonstrate that ADP-ribose exposure triggers neuronal ferroptosis.

214 Notably, low-dose ADP-ribose treatment exacerbated cortical neuron death induced by sublethal
215 doses of various ferroptotic inducers, including hemin (an oxidized form of heme), RSL3 (a
216 GPX4 inhibitor), or FIN56 (an agent that activates squalene synthetase), which was rescued by
217 Fer-1 (Fig. S6D). GPX4 converts lipid hydroperoxides to lipid alcohols and prevents ferroptosis
218 [13], and its expression is dependent on selenium availability (Fig. S6, E and F) [21]. Selenium dose-
219 dependently abrogated ADP-ribose-induced neuronal death (Fig. 3D). In addition, HT22 cells
220 expressing Q76A/Q145A mutant ENT2 showed reduced lipid peroxidation and cell death after
221 ADP-ribose treatment compared to wild-type cells (Fig.2L, and Fig. S6G). Thus, ADP-ribose
222 triggers neuronal ferroptosis by inducing lipid peroxidation.

223 The initiation and propagation of lipid peroxidation are dependent on Fe^{2+}-catalyzed Fenton
224 reactions [35]. Specifically, we observed that ADP-ribose exposure increased the Fe^{2+}/Fe^{3+} ratio in
225 HT22 cells (Fig. 3E), indicating that the Fe^{3+} generated after the reaction is reduced back to Fe^{2+}.
226 Cellular superoxide anions are known to modulate iron redox state and thereby induce
227 ferroptosis [9,36]. Indeed, superoxide anion assays confirmed that ADP-ribose exposure increased

228 superoxide anion production in HT22 cells (Fig. 3F). While electron transport chain (ETC)
229 dysfunction is typically associated with increased superoxide anions, ADP-ribose exposure had
230 no direct effect on ETC activity (Fig. S6H). These results suggest that ADP-ribose triggers
231 neuronal ferroptosis by accumulating superoxide anions.

232 **ADP-ribose triggers ferroptosis in a XO/DHODH-dependent manner**

233 To investigate the mechanisms underlying ADP-ribose-induced superoxide anion accumulation,
234 we performed untargeted metabolomics profiling of SH-SY5Y cells (Fig. S7, A to C;
235 Supplementary Table 4). Treatment with ADP-ribose enriched key intermediates in both purine
236 and pyrimidine biosynthesis pathways (Fig. 3G and Supplementary Table 5). Specifically, ADP-
237 ribose treatment elevated intracellula levels of deoxyinosine, inosine and hypoxanthine,
238 suggesting engagement of the inosine-hypoxanthine-XO purine catabolic pathway (Fig. 3G and
239 S4L). Hypoxanthine can be oxidated by xanthine oxidase (XO) to generate superoxide anions[37].
240 Accordingly, XO knockdown or inhibition with allopurinol[38] markedly reduced ADP-ribose-
241 induced superoxide production (Fig. S8, A and B). Moreover, blocking hypoxanthine production
242 through inhibition of purine nucleoside phosphorylase with forodesine [39] also protected murine
243 primary cortical neurons from ADP-ribose cytotoxicity (Fig. S8C).

244 Additionally, levels of glutamine, dihydroorotate and orotate accumulated under ADP-ribose
245 exposure, implicating activation of the glutamine-dihydroorotate-DHODH axis (Fig. 3G).
246 Dihydroorotate dehydrogenase (DHODH) catalyzes the oxidation of dihydroorotate to orotate
247 via ubiquinone with concomitant superoxide generation [40]. Accordingly, inhibiting DHODH with
248 either leflunomide or BAY-2402234, or depleting DHODH via shRNAs knockdown,
249 significantly reduced ADP-ribose-induced superoxide production and lipid peroxidation levels

250 (Fig. S8, C to E). Blocking glutamine uptake through GPNA treatment elicited comparable
251 effects (Fig. S8C).

252 Glutamine, the primary precursor for *de novo* purine and pyrimidine synthesis, was essential for
253 ADP-ribose-induced ferroptosis (Fig. S8F). Metabolic flux analyses using $^{15}N_2$-glutamine
254 revealed that ADP-ribose treatment substantially leads to intracellular accumulation of key
255 purine (IMP, inosine and hypoxanthine) and pyrimidine (aspartate, dihydroorotate and orotate)
256 intermediates derived from glutamine (Fig. 3, H and I; Fig. S9, A and D). Notably, downstream
257 purine and pyrimidine nucleotides incorporated less of the ^{15}N-label compared to precursors (Fig.
258 Fig. 3, H and I; Fig. S9, A and D). This ADP-ribose-induced purine and pyrimidine *de novo*
259 pathway can be explained by the reduced salvage pathway independently of metabolic enzyme
260 regulation upon ADP-ribose exposure in ^{13}C-flux analysis (Fig. S9, A to H). Collectively, these
261 results demonstrate that ADP-ribose triggers ferroptosis by co-opting the XO and DHODH arms
262 of purine and pyrimidine biosynthesis to generate cytotoxic ROS.

263 Simultaneous knockdown of XO and DHODH (Fig. S8A) or combined inhibition of
264 XO/DHODH with allopurinol/leflunomide markedly reduced ADP-ribose-induced di- and tri-
265 oxygenated phosphatidylethanolamines species (C18:0/C20:4 and C18:0/C22:4)[41] and ferroptotic
266 cell death (Fig. 3, J and K; Fig. S8G). Thus, in contrast to depleting the cysteine–GSH–GPX4
267 axis, ADP-ribose exposure remodels purine and pyrimidine metabolism through XO/DHODH to
268 excessively produce superoxide from hypoxanthine and dihydroorotate, triggering initiation and
269 propagation of lipid peroxidation and ferroptosis (Fig. S8H).

270 **ADP-ribose exposure induces neuronal ferroptosis *in vivo***

271 We next evaluated whether ADP-ribose induces *in vivo* XO/DHODH-dependent neuronal
272 ferroptosis. In *D. drosophila*, ADP-ribose feeding induced wing defects (Fig. S10A) and severely
273 impaired climbing ability linked to neurodegeneration (Fig. S10B). ADP-ribose also significantly
274 reduced fly survival (Fig. S10C). Consistent with our findings on ENT2 and metabolite
275 accumulation, pretreatment with allopurinol and leflunomide before ADP-ribose extended
276 lifespans (Fig. S10C). We overexpressed NUDT9 in TauR406W mutant flies using GAL4/UAS.
277 NUDT9 overexpression significantly reduced brain ADP-ribose levels and prolonged lifespans
278 (Fig. S10, D and E). Depletion of PARP1 or PARG in *D. drosophila* causes developmental arrest
279 before pupation, therefore, we treated flies with the PAPR1 degrader iRucaparib-AP6.
280 iRucaparib-AP6 treatment effectively blocked ADP-ribose production and extended lifespans of
281 TauR406W mutants (Fig. S10, F and G).

282 Utilizing rat organotypic hippocampal slice cultures (OHSCs), which preserve the integrity of
283 neuronal connections and supporting cells (Fig. 4A) [42], we found ADP-ribose treatment induced
284 extensive neuronal cell death by diphenyl-1-pyrenylphosphine and propidium iodide staining [43]
285 in the dentate gyrus (DG), CA1 and CA3 regions (Fig. 4, B to D, and Fig. S11, A to E).
286 Attenuating XO/DHODH with AAV-knockdown or co-treating with allopurinol/leflunomide
287 significantly reduced ADP-ribose toxicity, as did DFO and Lip-1 controls (Fig. 4, B to D, and
288 Fig. S11, A to E).

289 We investigated the effects of direct ADP-ribose microinjection into the mouse hippocampus and
290 cortex (Fig. 4E). Two days post-injection, ADP-ribose severely depleted neuronal numbers in the
291 cortex (Fig. 4F; for local magnification, see Fig. S12, A to D) and hippocampus regions (Fig. 4G;
292 for local magnification, see Fig. S13, A to D). Specifically, most CA1-CA3 neurons died while
293 DG neurons farther from the injection site were preserved (Fig. S13B). Critically, concurrent

294 injection of allopurinol and leflunomide significantly attenuated ADP-ribose-mediated
295 neurotoxicity in both the cortex (Fig. 4F; for local magnification, see Fig. S12C) and
296 hippocampus (Fig. 4G; for local magnification, see Fig. S13C). Thus, direct ADP-ribose
297 exposure *in vivo* induces neurological impairment by activating XO/DHODH-dependent
298 ferroptotic signaling pathways.

299 **ADP-ribose is responsible for ICH-induced cognitive decline in mice**

300 Intracerebral hemorrhage (ICH) induces oxidative stress and cognitive impairment in mice [21,44].
301 We utilized a collagenase-induced ICH model to assess whether ADP-ribose is responsible for
302 ICH-induced cognitive decline. ICH significantly increased ADP-ribose levels in hippocampal
303 neurons 24 hours post-ICH compared to sham controls (Fig. S14, A to C) and reduced CA1
304 neuron numbers 5 weeks later (Fig. 4H, and S14D), indicating that ICH elicits ADP-ribose
305 production and hippocampal neuronal death. We next assessed spatial memory via Morris water
306 maze (MWM) five weeks post-ICH (Fig. 4I). While escape latency decreased across training
307 days for all groups, ICH mice exhibited significantly poorer performance than sham controls
308 each day (Fig. S14, E and F), with no difference in swim velocity (Fig. S14G). In a probe trial,
309 sham mice spent more time in the target quadrant and crossed the platform location more often
310 than ICH mice (Fig. 4, J and K). Thus, ICH impairs spatial memory required for the MWM task.

311 To determine whether inhibiting ADP-ribose production alleviates ICH-induced cognitive
312 deficits, we knocked down PARP1 in neurons using AAV vectors. A 1:1 mixture of AAV-
313 SpCas9 (containing neuron-specific *Mecp2* promoter) and AAV-SpGuide (*lacZ*-targeting
314 sgRNAs as a negative control) was stereotactically injected into the hippocampus of adult male
315 mice (Fig. S15, A and B). Co-staining 3 weeks after viral injection showed ~85% co-
316 transduction efficiency of the two vectors (GFP-KASH^{+}/HA-Cas9^{+}) in hippocampal CA1

317 neurons (Fig. S15C). PARP1 protein levels were decreased by 75% in the hippocampus of mice
318 injected with *Parp1*-targeting vs *lacZ*-targeting sgRNAs (Fig. S15, D and E). We observed that
319 ADP-ribose levels were significantly decreased in PARP1 knockdown hippocampal neurons 24
320 hours post-ICH (5.61 pg/cell in controls vs 1.58 pg/cell in PARP1-KD, $P<0.0001$) (Fig. S15F).
321 In MWM training trials, PARP1 knockdown ICH mice had significantly reduced escape
322 latencies compared to controls (Fig. S15, G to I). During the probe trial, PARP1 knockdown ICH
323 mice spent more time in the target quadrant and crossed the platform location more often than
324 controls (Fig. 4, L to N). Thus, inhibiting ADP-ribose production improved ICH-induced spatial
325 memory deficits.

326 Further, to determine whether promoting ADP-ribose degradation alleviates ICH-induced
327 cognitive deficits, we administered intrahippocampal microinjections of recombinant human
328 NUDT9 proteins or heat-inactivated NUDT9 before ICH and on days 7 and 14 post-ICH (Fig.
329 4H). NUDT9 treatment significantly increased the number of surviving CA1 hippocampal
330 neurons 5 weeks after ICH compared to controls, consistent with the neuroprotective effects
331 observed with the ferroptosis inhibitor Lip-1 (Fig. 4H, and Fig. S14D). In MWM training trials,
332 ICH mice receiving NUDT9 proteins showed significantly reduced escape latencies versus those
333 receiving heat-denatured NUDT9 (Fig. S14, E and F). During the probe trial, ICH mice receiving
334 NUDT9 proteins spent more time in the target quadrant and crossed the platform location more
335 frequently than controls (Fig. 4, J and K). Collectively, these results demonstrate that promoting
336 ADP-ribose degradation through NUDT9 administration alleviated ICH-induced neuronal loss
337 and cognitive impairment, indicating blocking ADP-ribose signaling mitigates cognitive decline
338 from ICH.

339 **DISCUSSION**

340 In this study, we demonstrate that ADP-ribose, a product of NAD^+ consumption, induces
341 neuronal ferroptosis and is elevated in neurological disease models such as AD and stroke. Our
342 findings also revealed a complex interplay involving XO and DHODH in driving lipid
343 peroxidation and subsequent neuronal ferroptosis. Interventions blocking ADP-ribose signaling
344 alleviated cognitive decline in ICH models, highlighting the potential therapeutic significance of
345 targeting this pathway. Therefore, a therapeutic strategy involves supplementing NAD^+
346 availability while preventing ADP-ribose neuronal toxicity. To inhibit ADP-ribose accumulation,
347 we propose three approaches: 1) inhibiting NAD^+-consuming enzymes like PARP1 to block
348 ADP-ribose production; 2) depleting ADP-ribose with an ADPR hydrolase like NUDT9; 3)
349 inhibiting ADP-ribose-driven ROS generation with XO/DHODH inhibitors like allopurinol and
350 leflunomide.

351 While ADP-ribose-induced neuronal cell death relies on PARP1 activation, the mechanism
352 diverges from PAR-induced parthanatos[8]. Extracellular ADP-ribose directly binds to ENT2,
353 remodeling intracellular purine and pyrimidine metabolism. In neurons that predominantly
354 utilize salvage pathways for nucleosides synthesis rather than *de novo* pathways, ENT2 functions
355 as the high-affinity transport to fulfill nucleoside demands [45]. As ENT2 supports energy
356 homeostasis[46], deletion impairs mitochondrial bioenergetics and deteriorates neurological
357 dysfunction in mice[47]. We hypothesize that in cell types resistant to ADP-ribose-induced
358 ferroptosis, such as astrocytes, multiple nucleoside transport systems are engaged rather than sole
359 reliance on ENT2.

360 DHODH contributes to mitochondrial ROS production directly and indirectly by depositing
361 electrons onto CoQ to form $CoQH_2$ that is then re-oxidized by CIII/IV-mediated respiration[48].
362 Importantly, DHODH inhibitors like leflunomide or brequinar bind to the CoQ site of DHODH,

363 inhibiting both direct and indirect modes of mitochondrial ROS production[48,49]. However, the
364 physiological relevance of DHODH-induced ROS was previously unclear. Our study found that
365 DHODH-induced mitochondrial ROS promotes ER phosphatidylethanolamines peroxidation and
366 neuronal ferroptosis.

367 While DHODH inhibition was found to reduce ADP-ribose-induced mitochondrial ROS
368 production and lipid peroxidation in neurons, a recent study showed that DHODH protects
369 cancer cells from ferroptosis[50]. This discrepancy may stem from the different metabolic features
370 between cancer and neuronal cells: 1) cancer cells frequently overexpress DHODH to support
371 rapid proliferation via *de novo* pyrimidine synthesis, whereas neurons predominantly rely on the
372 salvage pathway for nucleic acid synthesis and DHODH is dispensable under normal
373 physiological conditions[51,52]; 2) cancer cells maintain high redox stress signaling threshold
374 compared to neurons, which exhibit low tolerance for oxidative stress and have high
375 phospholipid content in membranes, enhancing vulnerability to lipid peroxidation and
376 ferroptosis [53]; 3) neurons also appear to be intolerant of glutamine[54], which is essential for *de*
377 *novo* pyrimidine synthesis in cancer cells; 4) there may be off-target effects of DHODH
378 inhibitors not directly linked to DHODH itself[55]. Our study reveals that distinct metabolic
379 features determine cellular responses to ferroptotic insults.

380 **Limitations of the Study**

381 This study provides novel insights into the mechanisms of ADP-ribose signaling and neuronal
382 ferroptosis. However, there are some limitations that future work could address. First, our
383 findings that ADP-ribose induces neuronal cell death relies heavily on *in vitro* studies using
384 cultured cells and acute toxin exposures. Validating conclusions regarding ADP-ribose signaling
385 and their perturbation in rigorously characterized *in vivo* disease paradigms will strengthen the

386 pathophysiological relevance of our findings. Additionally, our findings suggest ADP-ribose
387 production transcends PARPs, as oxidatively stressed neurons release ADP-ribose independently
388 PARP1. Precisely characterizing how ADP-ribose production relates to specific NAD^+-
389 consuming enzymes, such as Sirtuins and SARM1, under different disease contexts remains an
390 important area for future study. Lastly, while our study focused on extracellular ADP-ribose
391 functions in neurons, TPP screening identified 40 intracellular proteins whose stability was
392 altered by ADP-ribose binding. Elucidating the spatio-temporal regulation and functional
393 consequences of intracellular ADP-ribose engagement with putative targets in neurons and
394 across diverse cell types, could provide novel mechanistic insights. Overall, continued
395 interrogation of ADP-ribose signaling in health and disease holds promise for advancing our
396 understanding and ability to intervene against neurological disorders.

397 **ACKNOWLEDGMENTS**

398 We thank Hamid Baniasadi (UT Southwestern Medical Center) for untargeted metabolomics and
399 target metabolomics analysis, Xiaoyu Wang (UT Southwestern Medical Center) for ADP-ribose
400 concentration analysis, Duojia Pan (UT Southwestern Medical Center) for feeding of Drosophila,
401 and Wei Peng (UT Southwestern Medical Center) for protein-molecule structure mock docking.
402 We thank Marcus Conrad (Helmholtz Zentrum München), Boyi Gan (University of Texas MD
403 Anderson Cancer Center), Xuejun Jiang (Sloan Kettering Institute), Yonghao Yu (UT
404 Southwestern Medical Center), Baiyun Wang (University of Washington) and Jiang Dai
405 (Jingwan Biomedical Technology Co., LTD) for helpful discussions and suggestions.

406 **Funding**

407 This work was supported by grants from the Guangdong Basic and Applied Basic Research
408 Foundation (2024A1515030060 to L.Y.), Chinese National Natural Science Foundation Projects

(81602422 to L.Y., 82001654 to P.C.), and NSFC Projects of international cooperation and exchanges (81820108011 to Q.Z.).

Author contributions

L.Y. conceived the study, designed, performed, and interpreted the experiments and wrote the manuscript. Most of the experiments were performed by L.Y., H.N., Y.H. and H.C.; P.C., G.L. and B.C. developed and performed bioinformatics and statistical analysis, and revised the manuscript; H.L., P.C., and F.Y. generated the fruit fly model and mouse model, and revised the manuscript; AD patient sample collection and analysis was carried out by Q.Z., H.N., B.C. and L.Y..

Competing Interests

The authors declare no competing interests.

Supplementary Tables

Supplementary Tables 1–8.

REFERENCES

1 Zhu, X. H., Lu, M., Lee, B. Y., Ugurbil, K. & Chen, W. In vivo NAD assay reveals the intracellular NAD contents and redox state in healthy human brain and their age dependences. *Proc Natl Acad Sci U S A* **112**, 2876-2881, doi:10.1073/pnas.1417921112 (2015).

2 Lautrup, S., Sinclair, D. A., Mattson, M. P. & Fang, E. F. NAD(+) in Brain Aging and Neurodegenerative Disorders. *Cell Metab* **30**, 630-655, doi:10.1016/j.cmet.2019.09.001 (2019).

3 Zapata-Perez, R., Wanders, R. J. A., van Karnebeek, C. D. M. & Houtkooper, R. H. NAD(+) homeostasis in human health and disease. *EMBO Mol Med*, e13943, doi:10.15252/emmm.202113943 (2021).

4 Kraus, W. L. PARPs and ADP-Ribosylation: 50 Years ... and Counting. *Mol Cell* **58**, 902-910, doi:10.1016/j.molcel.2015.06.006 (2015).

5 Cohen, M. S. & Chang, P. Insights into the biogenesis, function, and regulation of ADP-ribosylation. *Nat Chem Biol* **14**, 236-243, doi:10.1038/nchembio.2568 (2018).

6 Park, H., Kam, T. I., Dawson, T. M. & Dawson, V. L. Poly (ADP-ribose) (PAR)-dependent cell death in neurodegenerative diseases. *Int Rev Cell Mol Biol* **353**, 1-29, doi:10.1016/bs.ircmb.2019.12.009 (2020).

7 Cortes, U. *et al.* Depletion of the 110-kilodalton isoform of poly(ADP-ribose) glycohydrolase increases sensitivity to genotoxic and endotoxic stress in mice. *Mol Cell Biol* **24**, 7163-7178, doi:10.1128/MCB.24.16.7163-7178.2004 (2004).
8 Ying, W., Sevigny, M. B., Chen, Y. & Swanson, R. A. Poly(ADP-ribose) glycohydrolase mediates oxidative and excitotoxic neuronal death. *Proc Natl Acad Sci U S A* **98**, 12227-12232, doi:10.1073/pnas.211202598 (2001).
9 Dixon, S. J. *et al.* Ferroptosis: an iron-dependent form of nonapoptotic cell death. *Cell* **149**, 1060-1072, doi:10.1016/j.cell.2012.03.042 (2012).
10 Conrad, M. & Pratt, D. A. The chemical basis of ferroptosis. *Nat Chem Biol* **15**, 1137-1147, doi:10.1038/s41589-019-0408-1 (2019).
11 Jiang, X., Stockwell, B. R. & Conrad, M. Ferroptosis: mechanisms, biology and role in disease. *Nat Rev Mol Cell Biol* **22**, 266-282, doi:10.1038/s41580-020-00324-8 (2021).
12 Seiler, A. *et al.* Glutathione peroxidase 4 senses and translates oxidative stress into 12/15-lipoxygenase dependent- and AIF-mediated cell death. *Cell Metab* **8**, 237-248, doi:10.1016/j.cmet.2008.07.005 (2008).
13 Yang, W. S. *et al.* Regulation of ferroptotic cancer cell death by GPX4. *Cell* **156**, 317-331, doi:10.1016/j.cell.2013.12.010 (2014).
14 Friedmann Angeli, J. P. *et al.* Inactivation of the ferroptosis regulator Gpx4 triggers acute renal failure in mice. *Nat Cell Biol* **16**, 1180-1191, doi:10.1038/ncb3064 (2014).
15 Bersuker, K. *et al.* The CoQ oxidoreductase FSP1 acts parallel to GPX4 to inhibit ferroptosis. *Nature* **575**, 688-692, doi:10.1038/s41586-019-1705-2 (2019).
16 Doll, S. *et al.* FSP1 is a glutathione-independent ferroptosis suppressor. *Nature* **575**, 693-698, doi:10.1038/s41586-019-1707-0 (2019).
17 Kraft, V. A. N. *et al.* GTP Cyclohydrolase 1/Tetrahydrobiopterin Counteract Ferroptosis through Lipid Remodeling. *ACS Cent Sci* **6**, 41-53, doi:10.1021/acscentsci.9b01063 (2020).
18 Medina, C. B. *et al.* Metabolites released from apoptotic cells act as tissue messengers. *Nature* **580**, 130-135, doi:10.1038/s41586-020-2121-3 (2020).
19 Yu, B., Choi, B., Li, W. & Kim, D. H. Magnetic field boosted ferroptosis-like cell death and responsive MRI using hybrid vesicles for cancer immunotherapy. *Nat Commun* **11**, 3637, doi:10.1038/s41467-020-17380-5 (2020).
20 Zille, M. *et al.* Hemin-Induced Death Models Hemorrhagic Stroke and Is a Variant of Classical Neuronal Ferroptosis. *J Neurosci* **42**, 2065-2079, doi:10.1523/JNEUROSCI.0923-20.2021 (2022).
21 Alim, I. *et al.* Selenium Drives a Transcriptional Adaptive Program to Block Ferroptosis and Treat Stroke. *Cell* **177**, 1262-1279 e1225, doi:10.1016/j.cell.2019.03.032 (2019).
22 Hutton, M. *et al.* Association of missense and 5'-splice-site mutations in tau with the inherited dementia FTDP-17. *Nature* **393**, 702-705, doi:10.1038/31508 (1998).
23 Oakley, H. *et al.* Intraneuronal beta-amyloid aggregates, neurodegeneration, and neuron loss in transgenic mice with five familial Alzheimer's disease mutations: potential factors in amyloid plaque formation. *J Neurosci* **26**, 10129-10140, doi:10.1523/JNEUROSCI.1202-06.2006 (2006).
24 Radde, R. *et al.* Abeta42-driven cerebral amyloidosis in transgenic mice reveals early and robust pathology. *EMBO Rep* **7**, 940-946, doi:10.1038/sj.embor.7400784 (2006).
25 Slade, D. *et al.* The structure and catalytic mechanism of a poly(ADP-ribose) glycohydrolase. *Nature* **477**, 616-620, doi:10.1038/nature10404 (2011).

26 Pourfarjam, Y. *et al.* PARG has a robust endo-glycohydrolase activity that releases protein-free poly(ADP-ribose) chains. *Biochem Biophys Res Commun* **527**, 818-823, doi:10.1016/j.bbrc.2020.04.120 (2020).
27 Bonicalzi, M. E., Haince, J. F., Droit, A. & Poirier, G. G. Regulation of poly(ADP-ribose) metabolism by poly(ADP-ribose) glycohydrolase: where and when? *Cell Mol Life Sci* **62**, 739-750, doi:10.1007/s00018-004-4505-1 (2005).
28 Wang, S. *et al.* Uncoupling of PARP1 trapping and inhibition using selective PARP1 degradation. *Nat Chem Biol* **15**, 1223-1231, doi:10.1038/s41589-019-0379-2 (2019).
29 Huber, K. V. *et al.* Proteome-wide drug and metabolite interaction mapping by thermal-stability profiling. *Nat Methods* **12**, 1055-1057, doi:10.1038/nmeth.3590 (2015).
30 Kao, Y. H. *et al.* Targeting ENT1 and adenosine tone for the treatment of Huntington's disease. *Hum Mol Genet* **26**, 467-478, doi:10.1093/hmg/ddw402 (2017).
31 Governo, R. J., Deuchars, J., Baldwin, S. A. & King, A. E. Localization of the NBMPR-sensitive equilibrative nucleoside transporter, ENT1, in the rat dorsal root ganglion and lumbar spinal cord. *Brain Res* **1059**, 129-138, doi:10.1016/j.brainres.2005.08.017 (2005).
32 Anderson, C. M. *et al.* Distribution of equilibrative, nitrobenzylthioinosine-sensitive nucleoside transporters (ENT1) in brain. *J Neurochem* **73**, 867-873, doi:10.1046/j.1471-4159.1999.0730867.x (1999).
33 Wright, N. J. & Lee, S. Y. Structures of human ENT1 in complex with adenosine reuptake inhibitors. *Nat Struct Mol Biol* **26**, 599-606, doi:10.1038/s41594-019-0245-7 (2019).
34 Kovalevich, J., Santerre, M. & Langford, D. Considerations for the Use of SH-SY5Y Neuroblastoma Cells in Neurobiology. *Methods Mol Biol* **2311**, 9-23, doi:10.1007/978-1-0716-1437-2_2 (2021).
35 Stockwell, B. R. Ferroptosis turns 10: Emerging mechanisms, physiological functions, and therapeutic applications. *Cell* **185**, 2401-2421, doi:10.1016/j.cell.2022.06.003 (2022).
36 Stockwell, B. R. *et al.* Ferroptosis: A Regulated Cell Death Nexus Linking Metabolism, Redox Biology, and Disease. *Cell* **171**, 273-285, doi:10.1016/j.cell.2017.09.021 (2017).
37 Vergeade, A. *et al.* Xanthine oxidase contributes to mitochondrial ROS generation in an experimental model of cocaine-induced diastolic dysfunction. *J Cardiovasc Pharmacol* **60**, 538-543, doi:10.1097/FJC.0b013e318271223c (2012).
38 Luna, G., Dolzhenko, A. V. & Mancera, R. L. Inhibitors of Xanthine Oxidase: Scaffold Diversity and Structure-Based Drug Design. *ChemMedChem* **14**, 714-743, doi:10.1002/cmdc.201900034 (2019).
39 Balakrishnan, K., Nimmanapalli, R., Ravandi, F., Keating, M. J. & Gandhi, V. Forodesine, an inhibitor of purine nucleoside phosphorylase, induces apoptosis in chronic lymphocytic leukemia cells. *Blood* **108**, 2392-2398, doi:10.1182/blood-2006-03-007468 (2006).
40 Madak, J. T., Bankhead, A., 3rd, Cuthbertson, C. R., Showalter, H. D. & Neamati, N. Revisiting the role of dihydroorotate dehydrogenase as a therapeutic target for cancer. *Pharmacol Ther* **195**, 111-131, doi:10.1016/j.pharmthera.2018.10.012 (2019).
41 Kagan, V. E. *et al.* Oxidized arachidonic and adrenic PEs navigate cells to ferroptosis. *Nat Chem Biol* **13**, 81-90, doi:10.1038/nchembio.2238 (2017).
42 Noraberg, J. *et al.* Organotypic hippocampal slice cultures for studies of brain damage, neuroprotection and neurorepair. *Curr Drug Targets CNS Neurol Disord* **4**, 435-452, doi:10.2174/1568007054546108 (2005).

43 Okimotoa, Y., Watanabea, A., Nikia, E., Yamashitab, T. & Noguchia, N. A novel fluorescent probe diphenyl-1-pyrenylphosphine to follow lipid peroxidation in cell membranes. *FEBS Lett* **474**, 137-140, doi:10.1016/s0014-5793(00)01587-8 (2000).
44 Shi, E. *et al.* Chronic inflammation, cognitive impairment, and distal brain region alteration following intracerebral hemorrhage. *FASEB J* **33**, 9616-9626, doi:10.1096/fj.201900257R (2019).
45 Nagai, K., Nagasawa, K. & Fujimoto, S. Transport mechanisms for adenosine and uridine in primary-cultured rat cortical neurons and astrocytes. *Biochem Biophys Res Commun* **334**, 1343-1350, doi:10.1016/j.bbrc.2005.07.032 (2005).
46 Kropotov, A. *et al.* Equilibrative Nucleoside Transporters Mediate the Import of Nicotinamide Riboside and Nicotinic Acid Riboside into Human Cells. *Int J Mol Sci* **22**, doi:10.3390/ijms22031391 (2021).
47 Chen, C. Y. *et al.* Deletion of equilibrative nucleoside transporter 2 disturbs energy metabolism and exacerbates disease progression in an experimental model of Huntington's disease. *Neurobiol Dis* **177**, 106004, doi:10.1016/j.nbd.2023.106004 (2023).
48 Hey-Mogensen, M., Goncalves, R. L., Orr, A. L. & Brand, M. D. Production of superoxide/H2O2 by dihydroorotate dehydrogenase in rat skeletal muscle mitochondria. *Free Radic Biol Med* **72**, 149-155, doi:10.1016/j.freeradbiomed.2014.04.007 (2014).
49 Hail, N., Jr., Chen, P., Kepa, J. J., Bushman, L. R. & Shearn, C. Dihydroorotate dehydrogenase is required for N-(4-hydroxyphenyl)retinamide-induced reactive oxygen species production and apoptosis. *Free Radic Biol Med* **49**, 109-116, doi:10.1016/j.freeradbiomed.2010.04.006 (2010).
50 Mao, C. *et al.* DHODH-mediated ferroptosis defence is a targetable vulnerability in cancer. *Nature* **593**, 586-590, doi:10.1038/s41586-021-03539-7 (2021).
51 Qian, Y. *et al.* Elevated DHODH expression promotes cell proliferation via stabilizing beta-catenin in esophageal squamous cell carcinoma. *Cell Death Dis* **11**, 862, doi:10.1038/s41419-020-03044-1 (2020).
52 Bajzikova, M. *et al.* Reactivation of Dihydroorotate Dehydrogenase-Driven Pyrimidine Biosynthesis Restores Tumor Growth of Respiration-Deficient Cancer Cells. *Cell Metab* **29**, 399-416 e310, doi:10.1016/j.cmet.2018.10.014 (2019).
53 Reczek, C. R. & Chandel, N. S. ROS Promotes Cancer Cell Survival through Calcium Signaling. *Cancer Cell* **33**, 949-951, doi:10.1016/j.ccell.2018.05.010 (2018).
54 Johmura, Y. *et al.* Senolysis by glutaminolysis inhibition ameliorates various age-associated disorders. *Science* **371**, 265-270, doi:10.1126/science.abb5916 (2021).
55 Mishima, E. *et al.* DHODH inhibitors sensitize to ferroptosis by FSP1 inhibition. *Nature* **619**, E9-E18, doi:10.1038/s41586-023-06269-0 (2023).
56 Zhang, L. *et al.* Ras and Rap Signal Bidirectional Synaptic Plasticity via Distinct Subcellular Microdomains. *Neuron* **98**, 783-800 e784, doi:10.1016/j.neuron.2018.03.049 (2018).

METHODS

Ethics statement

576 All animal experiments were conducted in accordance with the 'Guide for the Care and Use of
577 Laboratory Animals' and 'Principles for the Utilization and Care of Vertebrate Animals', and
578 approved by the Institutional Human Research Ethics and Animal Care and Use Committee at
579 Wenzhou Medical University, Peking University and Peking University Shenzhen Hospital.
580 2×FAD and 5×FAD mice were from Yong Zhang (Peking university). We obtained human aged
581 55 to 70 years old lumbar CSF from the sample bank of the department of neurology, at Peking
582 University Shenzhen Hospital and First Affiliated Hospital of Wenzhou Medical University.
583 Diagnosis of Alzheimer's disease was established according to the NINCDS-ADRDA criteria. In
584 all patients and controls, lumbar puncture was performed, and CSF Chromogranin A measured.
585 Control subjects underwent CSF examination due to lower back pain or a tension-type headache.
586 The study protocol, including CSF examination, was approved by the Ethics Committee of
587 Peking University Shenzhen Hospital (# 2017S3-036). Informed consent was obtained from all
588 subjects or their relatives, and no compensation was provided for the sample collection.

589 **Cell culture, compounds and antibodies**

590 SH-SY5Y and HEK293T cells were purchased from ATCC, and HT22 cells were purchased
591 from Sigma. All cell lines were authenticated by STR profiling and tested for mycoplasma
592 contamination by GENEWIZ. Cells were cultured in DMEM supplemented with 10% FBS. Cells
593 were transfected with various plasmids using Lipofectamine 3000 (Invitrogen) reagent according
594 to the manufacturer's protocol. To provide a more intuitive and comprehensive overview of the
595 key resources utilized in this study, including compounds, plasmids, and antibodies, we have
596 included a detailed key resources table in the attached document named
597 Supplementary_Table_6_KEY RESOURCES TABLE.

598 **Isolation and culture of primary cortical neurons**

599 Primary cortical neurons were isolated from embryonic day 16.5 (E16.5) mice. The cortex
600 without meninges was carefully extracted from brain in the ice-cold HBSS and dissociated into
601 small pieces. We collected dissociated cortex through centrifugation for 3.5min at 500g. Then
602 the shredded cortex tissues were suspended and incubated in Enzyme solution (HBSS + 10U/mL
603 papain + 1mM $CaCl_2$ + 0.5 mM EDTA+ 1% DNase) for 10-15min with occasional mixing at
604 37℃. Then the digestion was ceased by 10% FBS and the cells were collected by centrifugation.
605 The single cells suspension was resuspended by 1mL DMEM and harvest by pipetting the
606 digested cortex tissue for 10 times and passing a 40 μm filter. Cells was harvest again,
607 resuspended by neurobasal medium (Gibco, USA) with 1% FBS and plated into PDL-coated 24-
608 wells plates (5×10^5/well). Three hours later, the medium was changed into neurobasal medium
609 with 2mM GlutaMAX (with or without 5μM ARAC, according to gestational day of mice; Gibco,
610 USA) but no FBS.
611 Neurons were maintained at 37°C with 5% CO_2 for 24 hours after plating prior to experiments
612 using immature primary cortical neurons. The neurons were validated through visual
613 morphology and positive expression of the neuronal marker NeuN. These immature cultures are
614 sensitive to 5mM glutamate/L-homocysteic acid (HCA)-induced ferroptosis. This cell death is
615 independent of ionotropic glutmate receptors, which do not fully develop until much later *in*
616 *vitro* (> 10 days). HCA-induced death in immature neuronal cultures is insensitive to MK801
617 (an ionic glutamate receptor antagonist; Sigma Aldrich) but is rescued by supplemental
618 cyst(e)ine.
619 For mature primary cortical neuronal cultures, every three days 50% media was changed and
620 cells were allowed to mature for 14 days before experimentation. Neurons were identified
621 through visual morphology. Mature neurons were sensitive to glutamate-induced excitotoxicity

622 as cell death was completely inhibited by MK801 treatment. Excitotoxicity was induced by
623 treating mature neurons with 100μM glutamate (Sigma Aldrich) in HBSS buffer for 1 hour at
624 37°C, followed by restoring the media at 37°C for 24 hours. The glutamate receptor antagonist
625 MK801 (10μM; Sigma Aldrich) was used as a positive control and added immediately after
626 glutamate treatment. Cell viability was assessed using the MTT assay (Promega).

627 **Drosophila culture and strains**

628 The transgenic flies were constructed to bear the different human tau constructs (tau, tauR406W)
629 under the control of a yeast upstream activating sequence (UAS). The human tau constructs were
630 cloned into the pUAST vector for the Gal4-inducible expression of transgenic pseuhosphorylated
631 tau in flies. Transgenic flies were generated by BestGene. Flies with the following genotypes
632 were utilized: 2N4R tau (UAS-tau/CyO) and 2N4R R406W (UAS-tauR406W/CyO). The
633 expression of tau protein was spatial controlled crossing transgenic flies with two driver lines
634 with specific expression to the nervous system (Elav-Gal4/CyO, Bloomington Stock Centre,
635 Indiana, USA, stock numbers 8765 and 25750). Only the progeny without curly phenotype was
636 analyzed (Elav-Gal4/UAS-tau; Elav-Gal4/UAS-tauR406W). All *Drosophila* stock and crosses
637 were reared on standard *Drosophila* media of sugar-cornmeal-yeast-agar and maintained at 23℃.
638 To induce the expression of the human tau, flies were raised at 29℃.

639 **CSF Sample Preparation**

640 After successful administration of spinal anesthesia, but prior to the administration of local
641 anesthetic, CSF (2 mL) was collected in a polypropylene tube and placed on ice. Samples were
642 immediately centrifuged at 3,000 × g for 10 min at 4°C to remove cells (Muller et al., 2014), and
643 the supernatant was aliquoted and stored at –80°C until analysis. Metabolites and lipids were
644 extracted from CSF samples using liquid–liquid extraction. Briefly, 500 μL of CSF were

645 concentrated to 50 μL and mixed with a fourfold volume of ice-cold chloroform/methanol (2:1,
646 v/v). After vertexing for 15 min at 4°C, the mixture was centrifuged at 13,000 × g for 15 min.
647 The upper aqueous phase (hydrophilic metabolites) and lower organic phase (hydrophobic
648 metabolites) were separately collected and evaporated at room temperature under vacuum. All
649 evaporated samples were stored at −80°C until high-performance liquid chromatography–mass
650 spectrometry (HPLC–MS) analysis.

651 ***In vitro* model of ferroptosis in neurons**

652 Cell death was induced in primary cortical neurons and hippocampal HT22 cells by treating with
653 100 μM hemin (Sigma Aldrich). The stock solution for hemin was dissolved in 0.1M NaOH.
654 Primary cortical neurons and HT22 hippocampal neuroblasts were exposed to 20 μM and and 2
655 μM erastin (dissolved in DMSO; Selleck Chemicals), respectively, to induce oxidative stress-
656 induced cell death by blocking xc^- transporters. Primary cortical neurons and HT22 hippocampal
657 neuroblast cells were exposed to 5mM L-homocysteic acid (HCA; Sigma Aldrich) dissolved in
658 MEM no phenol (Thermo Fisher Scientific), a structural analog of glutamate, to induce oxidative
659 stress – induced cell death by blocking the xc^- transporter. Sodium selenite (Sigma Aldrich),
660 dissolved in ddH_2O was applied to the media at varying concentrations. The time of addition of
661 hemin, erastin or HCA varied depending on experimental design; 24 hours after HCA treatment,
662 the cells were rinsed with warm PBS and cell viability was assessed by MTT assay (Promega) or
663 calcein-AM/ethidium homodimer-1 staining (Live/Dead assay, Thermo Fisher Scientific).
664 Similarly, other known ferroptosis inducers, RSL3 (Cayman Chemical) or FIN56 (Sigma Aldrich)
665 dissolved in DMSO, were used to induce cell death in primary cortical neurons. A minimum of
666 3 independent cell culture experiments were performed with studies involving ferroptosis of cells
667 *in vitro*.

668 **ADP-ribose concentration measurement**

669 **Analytical Processing**: 1×10^7 cells were harvested and washed 3 times with PBS. Add 1 ml of
670 80% methanol (pre-cooled at -20°C), shake well and centrifuge at high speed to remove protein
671 precipitates. Aliquot 500 μL 80% MeOH for blank and 490 μL 81.63% MeOH for standards.
672 Spike standards with appropriate amount of H_2O stock. Vortex 15 second. Transfer 200 μL of
673 blank and standards to the second Eppendorf tube. Aliquot 200 μL samples to the Eppendorf
674 tubes. Add 1 μL (10 ng/μL) of IS solution (IS final conc. = 50 ng/mL) to each sample including
675 blank, standards and samples, Vortex. Take 180 μL supernatant and transfer to HPLC vial with
676 insert. The supernatant was then analyzed by LC/MS/MS. **QTrap 6500 Parameters**:
677 Method: ADPr + pHilic UMP-13 IS 010920; Ion Source/Gas Parameters: CUR = 45, CAD =
678 High, IS = 2000, TEM = 500, GS1 = 70, GS2 = 70; Buffer A: dH2O + 20 mM NH4AC, Buffer B:
679 95%ACN +5% dH2O + 2 mM NH_4AC+ 0.1% HAC; flow rate 0.25 ml/min; column: Zic pHillic
680 PEEK coated 150 x2.1 mm 5 μM column; 0-1.5 min 80% B, 1.5-5.0 min gradient to 30% B, 5.0-
681 8.0 min 30% B, 8.0 - 9.0 min gradient to 80% B, 9.0 - 12.0 min 80% B; Compound transition
682 559.895 to 347.800; IS UMP-13 transition 336.092 to 102.000. **Explaining**: intracellular ADP-
683 ribose concentration (pg/cell) = total ADP-ribose mass in living cells /total living cell numbers;
684 extracellular ADP-ribose concentration (pg/cell) = total ADP-ribose mass in cell culture
685 medium/total cell numbers; ADP-ribose concentration in cerebrospinal fluid (CSF) (μg/ml) =
686 total ADP-ribose mass in CSF/ CSF volume.

687 **Determination of intracellular metabolite content**

688 Aspirate the medium and wash cells 2-3 times with PBS. Then add PBS, scrape the adherent
689 cells with a spatula, and count the cells. Take about 1×10^7 cells, centrifuge to remove the
690 supernatant. Add 1 ml of methanol/water (4:1) mixture (pre-cooled at -20°C), shake well and

691 centrifuge at high speed to remove protein precipitates. Centrifuge again and transfer the
692 supernatant to a new EP tube. The intracellular metabolites were measured by LC-MS QTrap
693 6500.

694 **Organotypic Hippocampal Slice Cultures**

695 OHSCs were cultured as previously described[56] with approval from Wenzhou Medical
696 University's IACUC. Briefly, Sprague Dawley rat pups (P6-P7) were rapidly decapitated, and the
697 hippocampus placed in ice-cold Hanks' Balanced Salt Solution (Gibco). 400 μm thick sections
698 were cut using a McIlwain tissue chopper and immediately plated on 0.4-mm pore size Millicell
699 cell culture membrane inserts (Millipore) in 800μL MEM culture Medium, containing: heat-
700 inactivated horse serum 20%, HEPES 30mM, glutamine 2mM, D-glucose 13mM, $NaHCO_3$
701 5mM, $CaCl_2$ 1mM, $MgSO_4$ 2mM, insulin 4 mg/L at pH 7.2 and osmolarity 320. Cultured slices
702 were maintained at 37°C and 5% CO_2. Medium was changed every 1-2 days.

703 **Excitotoxic Injury on OHSCs**

704 After 10-14 DIV, OHSCs were exposed to serum free media (SFM) consisting of 10 μM ADP-
705 ribose for 24 hr. Only healthy OHSCs defined as those with less than 5% cell death in all regions
706 (DG, CA3, CA1) of the hippocampus pre-injury were used for experiments. If chemical
707 compounds (*e.g.*, allopurinol/leflunomide and DFO) were added, they were added 3 hr before the
708 ADP-ribose.

709 **Analysis of Cell Death in Rat Brain Slices**

710 Quantification of cell death has been described previously[9]. Brightfield images of the
711 hippocampal cultures were taken before injury for identification of regions of interest (ROI)
712 including the dentate gyrus (DG), CA3 and CA1. Diphenyl-1-pyrenylphosphine (DPPP, SANTA
713 CRUZ BIOTECHNOLOGY) was used as a fluorescent signal for lipid peroxidation (ferroptosis

714 mark), and images were taken before the induction of injury and 24 hr following injury. For
715 DPPP/PI imaging, the cultures were transferred to SFM supplemented with 2 μM DPPP/PI. After
716 a 30min incubation, brightfield and DPPP/PI images were acquired. All images were captured on
717 a Leica DMi8 fluorescent microscope. Metamorphic image analysis software was used to
718 determine the ROI in the brightfield image, and this ROI was transferred to the DPPP/PI image
719 taken before and 24 hr after injury. Percentage cell death was expressed as the number of pixels
720 in the ROI above a threshold in the DPPP fluorescent image divided by the total number of
721 pixels in the ROI.

722 **Analysis of 4-HNE Production**

723 Lipid Peroxidation (4-HNE) Assay Kit (ab238538) is used for the quantitation of 4-HNE adduct
724 in protein samples. The standard curve is generated with 4-HNE-BSA. 50 μL standard or sample
725 were added to wells of 4-HNE Conjugate coated plate and incubated for 10 mins. Add 50 μL of
726 the diluted anti-4-HNE antibody and incubate for 1 h. Washing steps with 250 μL 1×Wash
727 Buffer. Add 100 μL diluted Secondary Antibody-HRP Conjugate per well and incubate for 1 h.
728 Wash as before with 1×Wash buffer. Add 100 μL of warm Substrate Solution and incubate for
729 20 mins. Stop the enzyme reaction by adding 100 μL of Stop Solution to each well. Read
730 absorbance immediately on a microplate reader using 450 nm.

731 **Analysis of Reactive Oxygen Species Production**

732 The day before the experiment, 5×10^5 cells/well were seeded in 6-well dishes (Corning). The
733 day of the experiment, cells were treated with test compounds for the indicated times; harvested
734 by trypsinization; resuspended in 500 μL Hanks Balanced Salt Solution (HBSS, Gibco)
735 containing H_2DCFDA (from abcam, ab113851); and incubated for 30 min at 37°C in a tissue

736 culture incubator. Cells were then resuspended in 500 μL buffer, and analyzed using a microplate
737 reader by fluorescence spectroscopy with excitation / emission at 485 nm/535 nm.

738 **Lipid Peroxidation Measurement**

739 Cells were seeded on 12-well plates and incubated overnight. The next day, cells were treated
740 with compounds for the indicated times, harvested by trypsinization and resuspended in 50 μL
741 lysis buffer (ab118970). Cell lysates were incubated with 10 μL MDA Color Reagent (ab233471)
742 for 30 min at 25°C in a water bath. Add 40 μL of Reaction Solution and incubate at room
743 temperature for 60 minutes. Monitor absorbance increase at 695 nm.

744 **Superoxide Anion Assay**

745 The method is based on the oxidation of luminol by superoxide anions resulting in the formation
746 of chemiluminescence light. This method utilizes a specific, non-toxic enhancer that amplifies
747 the chemiluminescent signal. Resuspend the cells in the Assay Medium (Sigma, A6105) to a
748 concentration of 5.0×10^5 to 1.0×10^6 cells/100 μL. Start the reaction by adding to each well 100
749 μL of Assay Buffer (Sigma, A5980) containing with 5% Luminol Solution (Sigma, L5034).
750 After 30min, measure the luminescence intensity by end point method.

751 **Identification of PE oxygenated products in cell lysates**

752 SH-SY5Y cells pre-treated with 10μM allopurinol and leflunomide for 1 hour were treated with
753 100μM ADP-ribose for 12 hours. Subsequently, the cells were resuspended in 25 mM HEPES
754 buffer (pH 7.4) containing 200 μM DTPA, sonicated, and prepared for experimentation. Lipids
755 were extracted using the Folch procedure. The PE fraction, containing both non-oxygenated and
756 oxygenated PE was obtained from those cells by normal phase LC/MS. PE and PEox (PEOOH)
757 were separated on a reverse phase column (Luna 3 μm C8 (2) 100A, 150 × 4.6 mm,
758 Phenomenex). The column was maintained at room temperature and eluted at a flow rate of 1.5

759 ml/min using an isocratic solvent system consisting of acetonitrile/H2O/trimethylamine/ acetic
760 acid (45/5/0.5/0.5, v/v/v/v). All solvents were of LC/MS grade. The eluant was monitored by UV
761 absorbance at 205 and 235nm on a Shimadzu HPLC system. Fractions containing PEox were
762 collected and identification was confirmed by mass spectrometry.
763 Oxygenated PEs were identified by MS/MS analysis utilizing an Orbitrap Fusion Lumos mass
764 spectrometer (ThermoFisher Scientific). The instrument was operated with an electrospray
765 ionization probe in negative polarity mode, with the following ion source conditions: spray
766 voltage = 3 kV, sheath gas = 55 (arbitrary unit), auxiliary gas = 10 (arb. unit), sweep gas = 0.5
767 (arb. unit), transfer tube temperature = 300 °C, vaporizer temperature = 200 °C, RF-Lens level =
768 20 %. Data acquisition was performed in data-dependant-MS^2 targeted-MS^3 mode, with a cycle
769 time setting of 3 s. For the MS scan event, the parameters were set as follow: ion detection using
770 the Orbitrap, mass resolution of 120,000, scan range of m/z 400 – 1800, and AGC target of 1e5.
771 The most intense ion was selected for the data-dependent MS^2 scan, with a dynamic exclusion of
772 9 s. An exclusion mass list for MS^2, consisting of m/z values of 130 background ions, was
773 created from solvent blank injection data. For the MS^2 scan event(s), the parameters were as
774 follows: quadrupole isolation of 1 Da, first mass of m/z 87, activation type of HCD, collision
775 energy of 28 % with a step of 8 %, ion detection using the Orbitrap, mass resolution of 15,000,
776 max injection time of 250 ms, and AGC target of 2e4. Product ions from a targeted mass list
777 were selected for MS^3 scanning. The target mass list for MS^3: 319.2279, 317.2123, 335.2228,
778 333.2072, 317.2123, 351.2159, 333.2054, 349.2003, 331.1898, 367.2126, 349.2021, 331.1916.
779 For the MS^3 scan event(s), the parameters were set as follows: top N = 4, isolation window = 2
780 Da, activation type = HCD, collision energy = 40 %, ion detection = Ion Trap, ion trap scan rate
781 = Rapid, max injection time = 500 ms, and AGC target = 3e4.

782 **Normal phase column separation and MS/MS analysis of phospholipids**

783 Phospholipids were separated on a normal phase column (Luna 3 μm Silica (2) 100Å, 150 × 2.0
784 mm, Phenomenex) at a flow rate of 0.2 mL/min on a Dionex Ultimate 3000 HPLC system. The
785 column was maintained at 35°C. Gradient elution was achieved using solvents A and B, both
786 containing 10 mM ammonium acetate and 0.5% triethylamine. Solvent A comprised
787 propanol:hexane:water (285:215:5, v/v/v) and solvent B sonsisted of propanol:hexane:water
788 (285:215:40, v/v/v), all of LC/MS grade. The elution profile began with an isocratic hold at 25%
789 B for 0.5 min, follwed by a linear gradient of 25–40% solvent B from 0.5 to 6.5 min, 40–55%
790 solvent B from 6.5–25 min, 55–70% solvent B from 25–38 min, 70%–100% solvent B from 38–
791 48 min. The column was then held isocratically at 100% solvent B for 7 min before returning to
792 initial conditions (25% B) over 15 min. The column was equilibrated at 25% B for an additional
793 5 min.

794 MS and MS/MS analysis of PLs was performed on a Q-Exactive hybrid-quadrupole-orbitrap
795 mass spectrometer (ThermoFisher Scientific) in negative ion mode. Full MS scans were
796 acquired at a resolution of 140,000, while MS^2 scan were acquired at a resolution of 17,500 in a
797 data-dependent manner. The MS scan range was set to 400–1800 m/z with a maximum injection
798 time of 128 ms using 1 microscan. For MS^2 analysis (high energy collisional dissociation
799 (HCD)), a maximum injection time of 500 ms was used, with a collision energy set to 24. An
800 inclusion list for phospholipids, including PE, PC, and CL, as well as their oxidized and
801 deuterated products, was employed. An isolation window of 1.0 Da was set for both MS and
802 MS^2 scans. The capillary spray voltage was set to 3.5 kV, and the capillary temperature was
803 maintained at 320 °C. The S-lens Rf level was adjusted to 60.

804 **Glutathione Assay**

805 Collect cells by centrifugation (i.e., 1,000-2,000 x g for 10 minutes at 4°C). The cell pellet can be
806 homogenized or sonicated in 1-2 mL of cold buffer (i.e., 50 mM MES or phosphate, pH 6-7,
807 containing 1 mM EDTA). Centrifuge at 10,000 x g for 15 minutes at 4°C. Remove the
808 supernatant and store on ice. Add an equal volume of the 1g/mL MPA Reagent to the sample and
809 mix by vertexing. Allow the mixture to stand at room temperature for five minutes and
810 centrifuge at >2,000 g for at least two minutes (a microfuge will be sufficient for the
811 centrifugation). Carefully collect the supernatant without disturbing the precipitate. Add 50 μL of
812 4M TEAM Reagent per ml of the supernatant and vortex immediately. The TEAM Reagent will
813 increase the pH of the sample. Read the plate at 405-414 nm after 25 minutes.

814 **^{13}C-tracers Uptake Assay**

815 SH-SY5Y cells were seeded in 6-well dishes (Corning) at a density of 5×10^5 cells per well. The
816 next day, cells were treated with 100 μM ADP-ribose for 3 hours; cells were washed twice in
817 prewarmed uptake buffer (137 mM choline chloride, 3 mM KCl, 1 mM $CaCl_2$, 1 mM $MgCl_2$,
818 5 mM D-glucose, 0.7 mM K_2HPO_4, and 10 mM HEPES pH 7.4) and then incubated for 10 min
819 at 37°C in 1 mL of uptake buffer to deplete cellular amino acids. At this point, in each well, the
820 buffer was replaced with 600 μL uptake buffer containing ADP-ribose and 50 μM of ^{13}C-tracers
821 (uridine cytidine, adenosine and cystine) and incubated for 3 min at 37°C. Cells were then
822 washed three times with ice-cold uptake buffer and lysed in 500 μL 0.1 M NaOH. This lysate
823 was measured by LC-MS QTrap 6500. All measurements were performed in triplicate for each
824 condition.

825 **Neuronal Cell Viability Measurements**

826 Cell viability was typically assessed in 96-well format by Cell Counting Kit-8 (CCK-8, Dojindo)
827 and alamarBlue™ Cell Viability Reagent Blue. Briefly, cells were seeded onto 96-well plates at

828 a density of 2×10^4 per well. Subsequently, cells exposed to 10 µl CCK-8 reagent (100 µl medium
829 per well) for 1 hour at 37 °C, 5% CO_2 in an incubator. The absorbance at a wavelength of 450
830 nm was determined using a FLUOstar Omega microplate reader (BMG Labtech). Alamar Blue
831 (Invitrogen) fluorescence (ex/em 530/590) measured on a Victor3 plate reader (Perkin Elmer). In
832 some experiments, Trypan blue dye exclusion counting was performed by using an automated
833 cell counter (ViCell, Beckman-Coulter). Cell viability under test conditions is reported as a
834 percentage relative to the negative control treatment.

835 **Iron Ion Analysis**

836 The ferrous and total iron was quantified using a spectrophotometric iron assay kit (BioVision,
837 Mountain View, CA) according to the manufacturer's directions. To quantify iron, samples were
838 treated with a reducing agent prior to incubation with Ferene S (Sigma-Aldrich, St. Louis, MO).
839 The optical density at 593 nm (OD_{593}) was measured after 1 h with a Synergy 2 microplate
840 reader (Biotek, Winooski, VT). A standard curve was routinely established (0 to 10 nmol of iron).

841 **ATP Concentration Analysis**

842 Cells were lysed in RIPA lysis buffer (50mM Tris-HCl pH 7.4, 150mM NaCl, 1% Nonidet-P40,
843 0.5% sodium deoxycholate, 1% SDS). After 20 min centrifugation at 12,000 rpm at 4 °C, the
844 supernatant was collected. The ATP concentration of the supernatant was assessed quantitatively
845 with the EnzyLight™ ATP Assay Kit (BioAssay Systems, Hayward, CA) according to the
846 instructions.

847 **Thermal Proteome Profiling (TPP)**

848 Lysis (M-PER buffer, Thermo Scientific, 89842 and 78501) was performed by five freeze–thaw
849 cycles using a 25 °C heating block and liquid nitrogen. Cell debris and precipitated proteins
850 were removed by centrifugation at 21,000g and 4 °C for 40 minutes. Supernatants were

851 transferred to new tubes and incubated with compounds at room temperature for 10 minutes then
852 placed on ice for 10 minutes. Equal volumes of soluble protein supernatants were transferred to
853 new tubes and subjected to gradient temperature denaturation for 3 minutes. Precipitated
854 proteins were removed by centrifugation at 21,000g and 4 °C for 40 minutes. First, the
855 supernatants samples were supplemented with reagents to contain a final concentration of 50 mM
856 TEAB, 0.1% SDS and 5 mM TCEP. Reduction was performed at 65 °C for 30 minutes.
857 Samples were then cooled down to room temperature and alkylated with 15 mM of
858 chloroacetamide for 30 minutes. Proteins were digested overnight with 1:40 Lys-C (Wako
859 Chemicals)-to-protein ratio. Consecutively, trypsin (Thermo Fisher Scientific) was added at a
860 1:70 enzyme-to-protein ratio for an 8-hour incubation at 37 °C. Finally, the same amount of
861 trypsin was added one more time for an overnight incubation. Resulting peptides were labeled
862 by 10-plex TMTpro tags (TMTpro, Thermo Fisher Scientific) using the same amount of
863 respective label for each sample. Eight melting points of two randomly selected cell lines were
864 combined in each TMT 10-plex set. The protein amounts were adjusted to contain the same total
865 protein amount for all cell lines throughout the TMT sets. An overview of the sets is given in
866 Supplementary Table 1. Labeling was performed according to the manufacturer's instructions
867 but with 2-hour incubation before quenching the TMT labeling reaction. Labeling efficiency
868 was determined by LC–MS/MS before mixing the TMT-labeled samples. Sample cleanup was
869 performed using solid-phase extraction Strata-X-C SPE columns (Phenomenex). Purified
870 peptides were dried in a vacuum centrifuge.

871 **RNA preparation and quantitative real-time PCR analysis**

872 Different mouse tissues or cells were lysed in Trizol (Invitrogen). Total RNA was recovered
873 from tissues following the manufacturer's protocol. Two micrograms of purified RNA from each

874 sample were reverse transcribed to single-stranded cDNA with All-In-One RT MasterMix
875 (catalogue no. G486, abm) The newly synthesized cDNA was mixed with TransStart Top Green
876 qPCR SuperMix (catalogue no.AQ131, Transgen Biotech) in a volume of 20 μL. For
877 Quantitative PCR, the Real Time PCR Detection system (ABI 7500) was using to detect each
878 gene in triplicate. Fold changes were analyzed (quantified) relative to the internal control gene
879 GAPDH based on the $2^{-\Delta\Delta CT}$ Method. Primer sequences used for qPCR are listed in
880 Supplementary Table 7.

881 **Lentivirus infection**

882 shRNA lentiviral vectors targeting human ENT1 (TRCN0000043643, TRCN0000043645,
883 TRCN0000043647) and ENT2 (TRCN0000043658, TRCN0000043659, TRCN0000043660)
884 were from Sigma. shRNA lentiviral vectors targeting mouse PARP1 (sc-29438-SH) and PARG
885 (sc-152026-SH), human XO (sc-41692-SH) and DHODH (sc-77142-SH) were from SANTA
886 CRUZ BIOTECHNOLOGY, INC.. Lentiviruses carrying overexpressing lentiviral vectors were
887 constructed by ourselves. The viruses were used to infect cells in the presence of Polybrene.
888 Forty-eight hours later, SH-SY5Y cells were cultured in medium containing puromycin for the
889 selection of stable clones. The clones stably knocking down ENT1/ENT2/XO/DHODH were
890 identified and verified by qPCR.

891 **Production of concentrated AAV vectors**

892 Adeno-associated viral (AAV) vectors for SpCas9 and guide RNAs were from Feng Zhang's Lab.
893 Adeno-associated virus carrying SpGuide vectors targeting mouse Parp1 (5′-
894 ACCCTGAAAGGGTAGCTTGT-3′), Ent1 (5′-CGACTACGTCTTTGCTCAAC-3′), Xo (5′-
895 CCAGCATGCAACGTACAGGG-3′), Dhodh (5′-TTGATCCAGAGTCGGCGCAC-3′) and
896 negative control LacZ (5′- TGCGAATACGCCCACGCGAT-3′) were constructed by ourselves.

897 High titer AAV-PHP.eB particles were produced using 1:2 ratio AAV-PHP.eB serotype
898 plasmids and pAdDF6 helper plasmid in HEK293FT and purified on heparin affinity column.
899 Briefly, HEK293FT cells were transfected with transgene plasmid, pUCmini-iCAP-PHP.eB and
900 pAd-deltaF6 (pAdDF6) at 1:2:1 ratio using PEI "MAX". Culture medium was collected after 48
901 h and filtered through a 0.45 μm PVDF filter (Millipore). Tittering of viral particles was done
902 with qPCR.

903 **Adeno-associated viral infection**

904 Mice were anesthetized by intraperitoneal (i.p.) injection of 100 mg/kg ketamine and 10 mg/kg
905 xylazine. Preemptive analgesia was given (Buprenex, 1 mg/kg, i.p.). Craniotomy was performed
906 according to approved procedures, and 1 μL of 1:1 AAV mixture (1×10^{13} vector genomes
907 (Vg)/ml) of sMecp2-SpCas9; 6×10^{12} Vg/ml of Parp1-sgRNA;) was stereotactically injected into
908 the hippocampus of adult mice with a coordinate of anterior/posterior, -2.0 mm; medial/lateral,
909 ±1.4 mm; and dorsal/ventral from skull, -1.7 mm. The skull was thinned using a dremel drill with
910 occasional cooling with saline, and the remaining dura was punctured using a glass micropipette
911 filled with the virus suspended in mineral oil. After each injection, the pipette was held in place
912 for 5 min before retraction to prevent leakage. The incision was sutured and 500 μL of saline was
913 injected subcutaneously to each mouse to avoid dehydration. Proper post-operative analgesics
914 (Meloxicam, 1–2 mg/kg) were administered for 3 d following surgery.

915 **Light Microscopy**

916 Phase contrast images were acquired using an AMG EVOS FL (Advanced Microscopy Group)
917 microscope equipped with a 10 × phase-contrast objective. Three independent fields were
918 acquired for each experimental condition. Representative samples from one field of view are
919 shown.

920 **Flow cytometry**

921 Cells fixed overnight with cold 70% ethanol were digested with RNase at 37℃ for 30 min and
922 stained with P.I., followed by flow cytometry analysis with a BD FACSVerse™ instrument.

923 **Collagenase-induced mouse model of ICH**

924 All surgeries were conducted under aseptic conditions by a skilled animal surgeon. ICH was
925 induced by intracerebral injection of collagenase in male C57BL/6 mice (10 to 12 weeks of age).
926 Female mice were not used to minimize the influence of sex steroids on recovery. Mice were
927 anesthetized with isoflurane (2 to 5%) and placed on a stereotaxic frame. During the procedure,
928 the animal's body temperature was maintained at 37℃ with a homeothermic blanket. Using a
929 nanomite syringe pump (Harvard Apparatus) and a Hamilton syringe, 1 μL of collagenase (0.05
930 U; Sigma) was infused into the right basal ganglia at a flow rate of 0.1 μL/min. The injection
931 coordinates were 2.3 mm lateral to midline and 0.5 mm anterior to bregma, and the needle was
932 inserted to a depth of 3.7 mm beneath the skull. In control animals, 1 μL of saline was infused.
933 Following infusion, the needle was removed after a 5 min pause to minimize overflow. The burr
934 hole was closed with bone wax, and the incision was sutured after surgery. In total, 500 μL of
935 saline was injected subcutaneously to each mouse to avoid dehydration.

936 **Animals and ADP-ribose injections**

937 Wild-type C57BL/6 mice were purchased from the Shanghai Laboratory Animal Center
938 (Shanghai, China). Both male and female mice at 2–4 months of age were used for experiment
939 unless otherwise stated. Mice were kept under a controlled temperature and a 12h light, 12h dark
940 cycle with free access to water and food in the animal facility of Wenzhou Medical University.
941 All experimental procedures and protocols were approved by the Animal Use and Care
942 Committee of Wenzhou Medical University. Adult mice were anesthetized by a cocktail of

943 ketamine (1.2 mg/kg body weight) − xylazine (0.8 mg/kg body weight) and placed on stereotaxic
944 frame (KOPF, California, USA). A final volume of 1μL ADP-ribose solution with a
945 concentration of 1mM was stereotactically injected into the hippocampus of adult mice with a
946 coordinate of anterior/posterior, -2.0 mm; medial/lateral, ±1.4 mm; and dorsal/ventral from skull,
947 -1.7 mm or into cortex with a coordinate of anterior/posterior, -2.0 mm; medial/lateral, ±1.4 mm;
948 and dorsal/ventral from skull, -1 mm.

949 **Hematoma Volume Measurement**

950 Mice were sacrificed 24h after ICH; the brains were removed and flash frozen in Freeze' IT
951 (Fisher Scientific). Coronal sections were sliced at 30 μm and placed directly on a glass slide. To
952 quantify hematoma volume, sections were digitized at standardized coronal levels. A blinded
953 user would measure the contours and hematoma from left and right hemisphere from each
954 section. Hematoma volume and swelling were measured and calculated using Axiovision
955 software (Carl Zeiss). Hematoma measurements were conducted on at least 5 independent brains
956 per group and hematoma volume was measured throughout the brain.

957 **Morris water maze assessment**

958 Cognitive function was evaluated using the Morris water maze (MWM). This test was conducted
959 in 2 periods. During the training period, mice introduced into a circular pool could escape by
960 finding a submerged hidden platform in the northeast quad- rant. In each trial, mice were
961 introduced to the pool through south or west sides and allowed to swim a maximum of 120
962 seconds to find the platform. Mice that successfully found the platform within 120 seconds were
963 allowed to stay on the platform for 10 seconds, whereas mice that failed to locate the platform
964 were placed on the platform and were also allowed to stay for 10 seconds. The training was
965 conducted in 3 trials per session, with 1 sessions/d for 5 days. The swimming velocity, escape

966 latency, and total distance swum during a trial were recorded. The water temperature in the pool
967 was maintained at 24°C during the test. On the sixth day, the platform was removed, and a single
968 trial was conducted by introducing the mice to the pool through the southwest quadrant. Each
969 mouse was allowed to swim for 120 seconds, during which the time spent in the target quadrant
970 and crossing times of the target platform were recorded. An EthoVision 3.1 tracking system
971 (Noldus Information Technology, Wageningen) was used for recording and analyzing data.

972 **Immunohistochemistry**

973 Mice were euthanized by CO_2 overdose and perfused with intracardial injection of ice-cold PBS
974 and 4% PFA (paraformaldehyde) in PBS. Brains were collected and postfixed with 4% PFA for
975 48 hr. Postfixed brains were cryoprotected with 30% sucrose solution in PBS for 72 hr and cut
976 into 18-μm-thick sections with a cryostat. Brain sections were serially collected and stored at -
977 20 ℃ . The primary antibody NeuN (Abcam, ab177487, 1:5000) was used for
978 immunohistochemical analyses. Alexa Fluor 555mm or 647mm secondary antibodies from
979 Jackson ImmunoResearch Laboratories were used at 1:5000 dilution for fluorescence. Nuclei
980 were counterstained with DAPI. Images were captured and examined by using a Leica DMi8
981 fluorescent microscope. ImageJ was used for cell counting.

982 **Statistics and reproducibility**

983 Experimental data were analyzed and processed using Excel (2016) and plotted with GraphPad
984 Prism 9.4.0 (GraphPad Software). Statistical analyses were conducted using unpaired two-tailed
985 t-tests and one-way ANOVA with Dunnett correction for multiple comparisons. For comparisons
986 between two groups, either an unpaired two-tailed *t*-test or Mann–Whitney test was employed.
987 For comparisons involving more than two groups, Kruskal–Wallis one-way ANOVA followed
988 by Dunn's multiple comparison tests or a two-way ANOVA followed by Bonferroni *post hoc*

989 tests was utilized. Survival curves were derived from Kaplan–Meier estimates and compared
990 using log-rank tests. All results are shown as the mean ± s.e.m. of multiple independent
991 experiments, not technical replicates. The number of experiments, sample size and statistic tests
992 used are detailed in the respective figure legends. Sample size was not predetermined using any
993 statistical method. Animals were randomly assigned to experimental groups to ensure unbiased
994 group allocation. The order of experimental conditions or stimulus presentation was not
995 randomized. No data were excluded from the analyses. The investigators were not blinded to
996 group allocation during experiments and outcome assessment. All statistical tests were conducted
997 on a two-sided basis, with P values <0.05 considered statistically significant.

998 **Reporting summary**

999 Further information on research design is available in the Nature Portfolio Reporting Summary
1000 linked to this article.

1001 **Data availability**

1002 All data supporting the findings of this study are available within the paper. Mass spectrometry
1003 data have been deposited in ProteomeXchange with the primary accession code PXD053136 and
1004 PXD053139. This paper does not report any original code. All other data supporting the findings
1005 of this study are available from the corresponding author on reasonable request. Source data are
1006 provided with this paper.

1007 **Figure legends**

1008 **Fig.1 ADP-ribose is toxic to neurons and upregulated in neurological diseases**

1009 A. Schematic conditioned medium preparation. EMX-A14 murine primary cortical neurons
1010 were treated with 100 μM hemin for 6 hours, followed by replacement with fresh medium for

1011 6 hours. Conditioned medium was concentrated (original), heated or filtered to generate
1012 fractions (>1,000 Da or <1,000 Da).

1013 B. Primary cortical neurons were treated with conditioned medium for 24 hours and cell
1014 viability assessed by CCK-8 assay. Kruskal–Wallis one-way ANOVA followed by Dunn's
1015 multiple comparison tests.

1016 C. Mature primary cortical neurons treated with 100 μM hemin for 6 hours. Extracellular ADP-
1017 ribose levels determined by LC-MS/MS (QTRAP 6500). Student's *t*-test with Welch's
1018 correction.

1019 D. Intracellular ADP-ribose levels in mature primary cortical neurons treated with 100 μM
1020 hemin for 6 hours. Student's *t*-test with Welch's correction.

1021 E. Viability of primary cortical neurons (plating 24 hours) was assessed after 24 hours treatment
1022 with ADP-ribose doses.

1023 F. Viability of mature cortical neurons (plating 2 weeks) treated with 100μM ADP-ribose over
1024 time.

1025 G. Viability of mature primary cortical neurons exposed to PAR, ADP-ribose, AMP, or ribose
1026 5-phosphate (R5P) for 24 hours. Kruskal–Wallis one-way ANOVA followed by Dunn's
1027 multiple comparison tests.

1028 H. Relative ADP-ribose levels in tauR406W and wild-type fruit fly brains measured by QTRAP
1029 6500 LC-MS/MS. n=50 flies. Mann–Whitney test.

1030 I. Hippocampal neuronal ADP-ribose levels in APP/PS1 and 5×FAD mice vs age. n=6. Two-
1031 way ANOVA (mouse strain × age) followed by Bonferroni *post hoc* tests.

1032 J. Cortical neuronal ADP-ribose levels in 6-month-old APP/PS1 and 5×FAD mice and wild-
1033 type littermate controls. n=6. Kruskal–Wallis one-way ANOVA followed by Dunn's
1034 multiple comparison tests.
1035 K. Hippocampal neuronal ADP-ribose levels in 6-month-old APP/PS1 and 5×FAD mice and
1036 wild-type littermate controls. n=6. Kruskal–Wallis one-way ANOVA followed by Dunn's
1037 multiple comparison tests.
1038 L. Cerebrospinal fluid (CSF) ADP-ribose levels were determined by QTRAP 6500 LC-MS/MS
1039 in healthy controls (n = 196) and patients with AD (n = 207). Mann–Whitney test.
1040 All data are means ± SEM. *, $P < 0.01$; x, no significant difference. See also Figures S1 and S2.
1041 Statistics source data can be found in Supplementary Table 2.

1042 **Fig.2 ADP-ribose is produced by the PARP1-PARG axis and directly targets ENT2**

1043 A. Primary cortical neurons isolated from the mice with neuron-specific *Parp1* knockdown were
1044 treated with 100 μM hemin. After 6 hours, the intracellular ADP-ribose levels were
1045 determined by QTRAP 6500 LC-MS/MS.
1046 B. Primary cortical neurons isolated from the mice with neuron-specific *Parp1* knockdown were
1047 treated with 100 μM hemin. After 6 hours, the NAD^+ levels were measured by NAD/NADH
1048 Assay Kit (ab65348).
1049 C. Primary cortical neurons isolated from the mice with neuron-specific *Parp1* knockdown were
1050 cultured for 12 hours in cystine-free media. The intracellular ADP-ribose levels were
1051 determined by QTRAP 6500 LC-MS/MS.
1052 D. Hippocampal HT22 neurons were pretreated with 0.1μM iRucaparib-AP6 (PROTAC PARP1
1053 degrader) or 2μM PDD (PARG inhibitor) for 1 hour, then treated with 5μM erastin or 5mM

1054 glutamate. After 8 hours, the cell lysates were subject to western blotting with anti-PAR
1055 antibodies. Quantification of total PAR levels in neuronal cells under oxidative stress (below).

1056 E. Primary cortical neurons were pre-treated with 0.1μM iRucaparib-AP6 or 2μM PDD for 1
1057 hour, then exposed to 100μM hemin for 6 hours, followed by culture in hemin-free medium
1058 for 6 hours. Conditioned medium from lane 4 was treated with 1 μg/ml ADP-ribose
1059 hydrolase NUDT9 (ab107153) to eliminate ADP-ribose prior to measurement of its
1060 concentration.

1061 F. Primary cortical neuronal viability assessed after culture with conditioned media from (E) for
1062 24 hours.

1063 G. Total SH-SY5Y proteins treated with or without 10μM ADP-ribose and analyzed by TMT10
1064 for thermal stability changes.

1065 H. Recombinant ENT2 or SLC7A11 incubated with ADP-ribose doses for 10 mins at room
1066 temperature then denatured at 60°C for 3 min and western blotted for stability.

1067 I. ^{13}C-uridine (Uri, 50 μM) or ^{13}C-cytidine (Cyt, 50 μM) uptake by SH-SY5Y cells pretreated
1068 with 100 μM ADP-ribose for 3 hours. ^{13}C-cystine (Cys, 50 μM) as a negative control.

1069 J. Detection of binding between *E. coli*-derived ENT2 wild-type (WT) or Q76A/Q145A mutant
1070 (mt) and ADP-ribose by thermal shift assay.

1071 K. HT22 cells stably expressing ENT2-WT or ENT2-mt were pretreated with 100 μM ADP-
1072 ribose for 3 hours, and the uptake of ^{13}C-uridine (50 μM) was measured.

1073 L. HT22 cells stably expressing ENT2-WT or ENT2-mt were treated with 100 μM ADP-ribose
1074 for 24 hours and cell viability was measured by CCK-8 assay.

1075 M. SH-SY5Y cells stably expressing the indicated shRNAs were treated with 100μM ADP-
1076 ribose for 24 hours and cell viability assessed by by CCK-8 assay.

1077 N. SH-SY5Y cells were differentiated through 6 days of treatment with 10 μM all-trans-retinoic
1078 acid (RA). Differentiated SH-SY5Y cells expressing the indicated plasmids were treated with
1079 100μM ADP-ribose for 24 hours before assessing cell viability.

1080 Data are means ± SEM of three independent experiments. Kruskal–Wallis one-way ANOVA
1081 followed by Dunn's multiple comparison tests. *, $P < 0.01$; x, no significant difference. See also
1082 Figures S3 to S5. Statistics source data can be found in Supplementary Table 2.

1083 **Fig.3 ADP-ribose triggers neuronal ferroptosis in a XO/DHODH-dependent manner**

1084 A. Quantification of primary cortical neurons viability after 24 hours of indicated treatment.
1085 ADP-ribose, 100μM; DFO, deferoxamine, a ferroptosis inhibitor, 100μM; CQ, chloroquine,
1086 an autophagy inhibitor, 10μM; ZVF, Z-VAD-FMK, a pan-caspase inhibitor, 10μM; Nec-1,
1087 Necrostain-1, a necroptosis inhibitor, 10μM.

1088 B. 4-HNE levels in primary cortical neurons exposed to 100μM ADP-ribose for 12 hours,
1089 measured by 4-HNE assay kit (ab238538).

1090 C. Cultured mature cortical neuron viability at 24 hours with treatments. Fer-1, ferrostatin-1, a
1091 ferroptosis inhibitor.

1092 D. Cultured primary cortical neuron viability at 24 hours with treatments.

1093 E. Fe^{2+}/Fe^{3+} ratio was measured in HT22 cells treated with 100μM ADP-ribose for 12 hours.

1094 F. Superoxide level was measured in HT22 cells treated with 100μM ADP-ribose for 12 hours.

1095 G. SH-SY5Y metabolomics identified altered purine and pyrimidine metabolites after 100μM
1096 ADP-ribose exposure for 12 hours. The change fold of metabolites under ADP-ribose
1097 treatment was labeled in purple number.

1098 H. Mass isotopomer analysis of aspartate (m+1), dihydroorotate (m+1/2), orotate (m+1/2),
1099 UMP (m+1/2) and CMP (m+1/2) in HT22 cells cultured with 3 mM $^{15}N_2$-glutamine and
1100 100μM ADP-ribose for 12 hours.
1101 I. Mass isotopomer analysis of IMP (m+2/3), inosine(m+2/3), hypoxanthine(m+2/3), XMP
1102 (m+2/3), AMP (m+2/3) and GMP (m+2/3/4) in HT22 cells cultured with 3 mM $^{15}N_2$-
1103 glutamine and 100μM ADP-ribose for 12 hours.
1104 J. SH-SY5Y cells stably expressing the indicated shRNAs or pre-treated with 10μM allopurinol
1105 and leflunomide for 1 hour, were treated with 100μM ADP-ribose for 12 hours. The levels of
1106 di- and tri-oxygenated PE-(C18:0/C20:4) and PE-(C18:0/C22:4) were detected by MS/MS.
1107 K. Differentiated SH-SY5Y cells stably expressing the indicated shRNAs or pre-treated with
1108 10μM allopurinol and leflunomide for 1 hour were treated with 100μM ADP-ribose and the
1109 cell viability was tested after 24 hours.
1110 Data are means ± SEM of three independent experiments. Kruskal–Wallis one-way ANOVA
1111 followed by Dunn's multiple comparison tests in A-D and H-J. Student's *t*-test with Welch's
1112 correction in E and F. *, $P < 0.01$; x, no significant difference. See also Figures S6 to S9.
1113 Statistics source data can be found in Supplementary Table 2.

1114 **Fig.4 ADP-ribose exposure induces neuronal ferroptosis *in vivo* and is responsible for ICH-**
1115 **induced cognitive decline in mice**
1116 A. Cartoon outline of rat organotypic hippocampal slice culture procedure.
1117 B. Organotypic hippocampal slices were pre-treated with 10 μM allopurinol/leflunomide or 100
1118 μM DFO for 3 hours, then exposed to 10 μM ADP-ribose for 7 days. Slices were stained with
1119 the positive staining diphenyl-1-pyrenylphosphine (DPPP) and the number of positively
1120 stained cells in the CA1 region was quantified.

1121 C. Positively stained cells were quantified in the CA3 region of slices treated as in (B).

1122 D. Positively stained cells were quantified in the dentrate gyrus region of slices treated as in (B).

1123 E. Schematic diagram showing the microinjection of 1μL ADP-ribose (1mM),
1124 allopurinol/leflunomide (200μM) and Lip-1 (40μM) into the cerebral cortex and
1125 hippocampus of mice. Lip-1, liproxstatin-1, a ferroptosis inhibitor.

1126 F. Cortical neuronal damage from ADP-ribose was characterized by counting NeuN-positive
1127 cells in the cortex (*n*=5 mice/group). Representative microscopic fluorescence imaging of
1128 cortical neurons from 1 of 5 mice per condition. Scale bar, 40μm.

1129 G. Histogram of neuronal counts in CA1-3 regions of hippocampus from mice treated as in (E)
1130 (*n*=5 mice/group). Representative microscopic fluorescence imaging of hippocampal neurons
1131 from 1 of 5 mice per condition. Scale bar, 350μm.

1132 H. Hippocampal CA1 neuronal counts at 5 weeks post-ICH by measuring NeuN-positive cells.
1133 Mice received ipsilateral (relative to the collagenase-infused side) hippocampal
1134 microinjections of 1μL NUDT9 (1 μg/μL) or Lip-1 (40 μM) 1 day before ICH and on days
1135 7/14 post-ICH.

1136 I. Schema of Morris water maze paradigm used to assess spatial learning and memory
1137 performance at 5 weeks post-ICH. Mice received ipsilateral hippocampal microinjections of
1138 1μg NUDT9 or heat-denatured NUDT9 one day before ICH and on days 7/14 post-ICH.

1139 J. Statistical results measuring time spent in the target quadrant during the probe trial.

1140 K. Counting the times of crossing the target platform area during the probe trial.

1141 L. Schema of MWM paradigm for PARP1 knockdown ICH mice. AAV-SpCas9 (*Mecp2*
1142 promoter) and AAV-SpGuide (*Parp1*- or *lacZ* (control)-targeting sgRNAs) were injected into

1143 the ipsilateral hippocampus 4 weeks before ICH (induced 1 month after AAV injection) to
1144 knock down PARP1.
1145 M. Statistical results measuring time spent in the target quadrant during the probe test.
1146 N. Counting the times of crossing the target platform area during the probe test.
1147 Data shown are means ± SD and are analyzed using two-way ANOVA (brain region × drug
1148 treatment) followed by Bonferroni *post hoc* tests in B-D; Data shown are means ± SEM and are
1149 analyzed using Kruskal–Wallis one-way ANOVA followed by Dunn's multiple comparison tests
1150 in F-N. n=5 mice; *, $P < 0.01$. See also Figures S10 to S15. Statistics source data can be found in
1151 Supplementary Table 2.

Fig.1

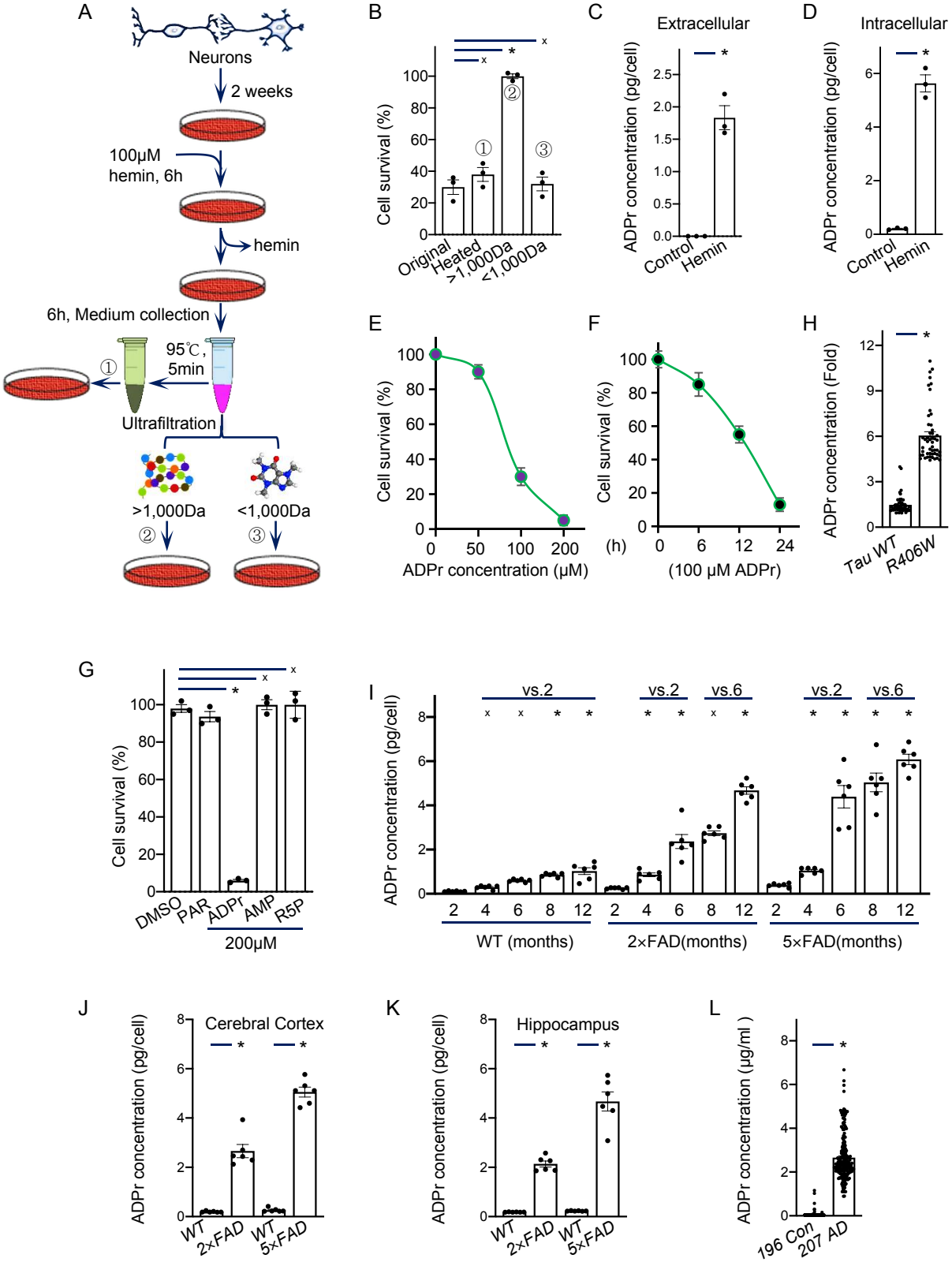
A
Neurons
2 weeks
100μM
hemin, 6h
hemin
6h, Medium collection
95℃,
5min
Ultrafiltration
>1,000Da
<1,000Da
B
Cell survival (%)
Original
Heated
>1,000Da
<1,000Da
C
Extracellular
ADPr concentration (pg/cell)
Control
Hemin
D
Intracellular
ADPr concentration (pg/cell)
Control
Hemin
E
Cell survival (%)
ADPr concentration (μM)
F
Cell survival (%)
(h)
(100 μM ADPr)
H
ADPr concentration (Fold)
Tau WT
R406W
G
Cell survival (%)
DMSO
PAR
ADPr
AMP
R5P
200μM
I
ADPr concentration (pg/cell)
vs.2
vs.2
vs.6
vs.2
vs.6
WT (months)
2×FAD(months)
5×FAD(months)
J
Cerebral Cortex
ADPr concentration (pg/cell)
WT
2×FAD
WT
5×FAD
K
Hippocampus
ADPr concentration (pg/cell)
WT
2×FAD
WT
5×FAD
L
ADPr concentration (μg/ml)
196 Con
207 AD

Fig.2

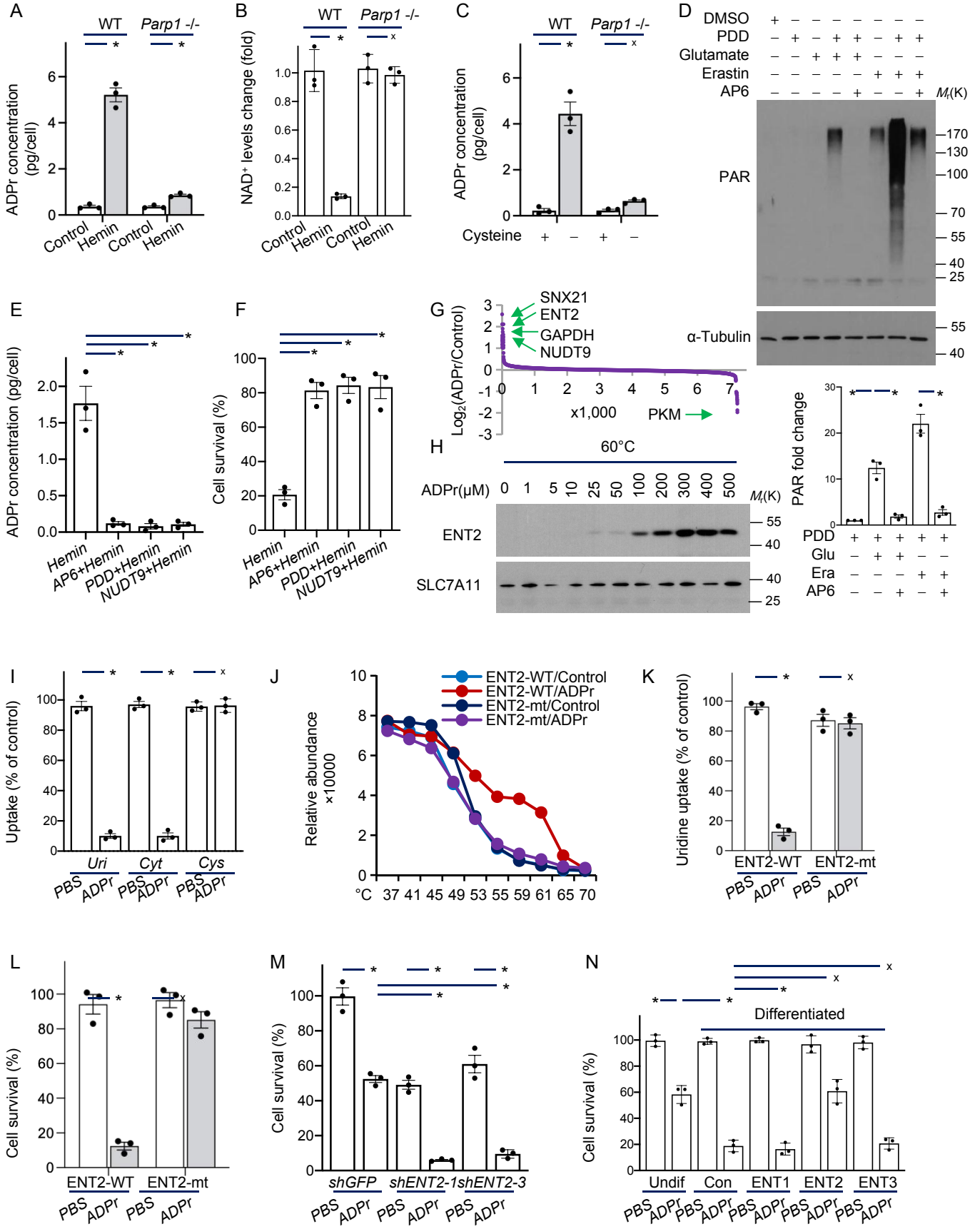
A
WT
Parp1 -/-
ADPr concentration (pg/cell)
Control
Hemin
B
NAD+ levels change (fold)
C
Cysteine
D
DMSO
PDD
Glutamate
Erastin
AP6
Mr(K)
PAR
α-Tubulin
E
Hemin
AP6+Hemin
PDD+Hemin
NUDT9+Hemin
F
Cell survival (%)
G
SNX21
ENT2
GAPDH
NUDT9
Log2(ADPr/Control)
x1,000
PKM
H
60°C
ADPr(μM)
ENT2
SLC7A11
PAR fold change
Glu
Era
I
Uptake (% of control)
Uri
Cyt
Cys
PBS
ADPr
J
ENT2-WT/Control
ENT2-WT/ADPr
ENT2-mt/Control
ENT2-mt/ADPr
Relative abundance ×10000
°C
K
Uridine uptake (% of control)
ENT2-WT
ENT2-mt
L
M
shGFP
shENT2-1
shENT2-3
N
Differentiated
Undif
Con
ENT1
ENT2
ENT3

Fig.3

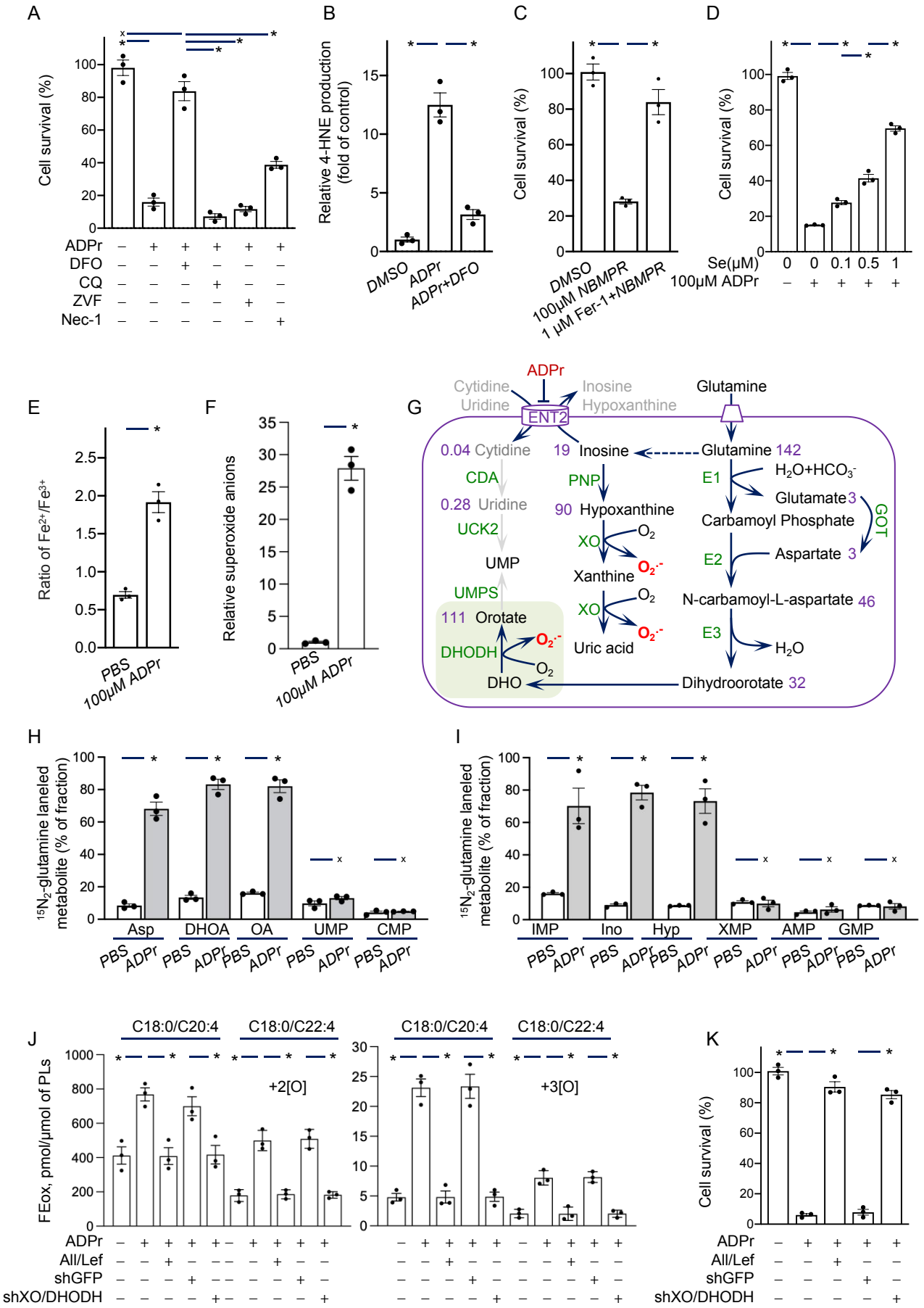
A
Cell survival (%)
ADPr
DFO
CQ
ZVF
Nec-1
B
Relative 4-HNE production (fold of control)
DMSO
ADPr
ADPr+DFO
C
Cell survival (%)
DMSO
100μM NBMPR
1 μM Fer-1+NBMPR
D
Cell survival (%)
Se(μM)
100μM ADPr
E
Ratio of Fe2+/Fe3+
PBS
100μM ADPr
F
Relative superoxide anions
PBS
100μM ADPr
G
ADPr
Cytidine
Uridine
Inosine
Hypoxanthine
ENT2
Glutamine
0.04 Cytidine
19 Inosine
Glutamine 142
CDA
PNP
E1
H2O+HCO3-
0.28 Uridine
90 Hypoxanthine
Glutamate 3
GOT
UCK2
XO
O2
Carbamoyl Phosphate
UMP
Xanthine
O2·-
E2
Aspartate 3
UMPS
N-carbamoyl-L-aspartate 46
111 Orotate
Uric acid
E3
DHODH
H2O
DHO
Dihydroorotate 32
H
15N2-glutamine laneled metabolite (% of fraction)
Asp
DHOA
OA
UMP
CMP
PBS
ADPr
I
15N2-glutamine laneled metabolite (% of fraction)
IMP
Ino
Hyp
XMP
AMP
GMP
J
C18:0/C20:4
C18:0/C22:4
FEox, pmol/μmol of PLs
+2[O]
+3[O]
ADPr
All/Lef
shGFP
shXO/DHODH
K
Cell survival (%)

Fig.4

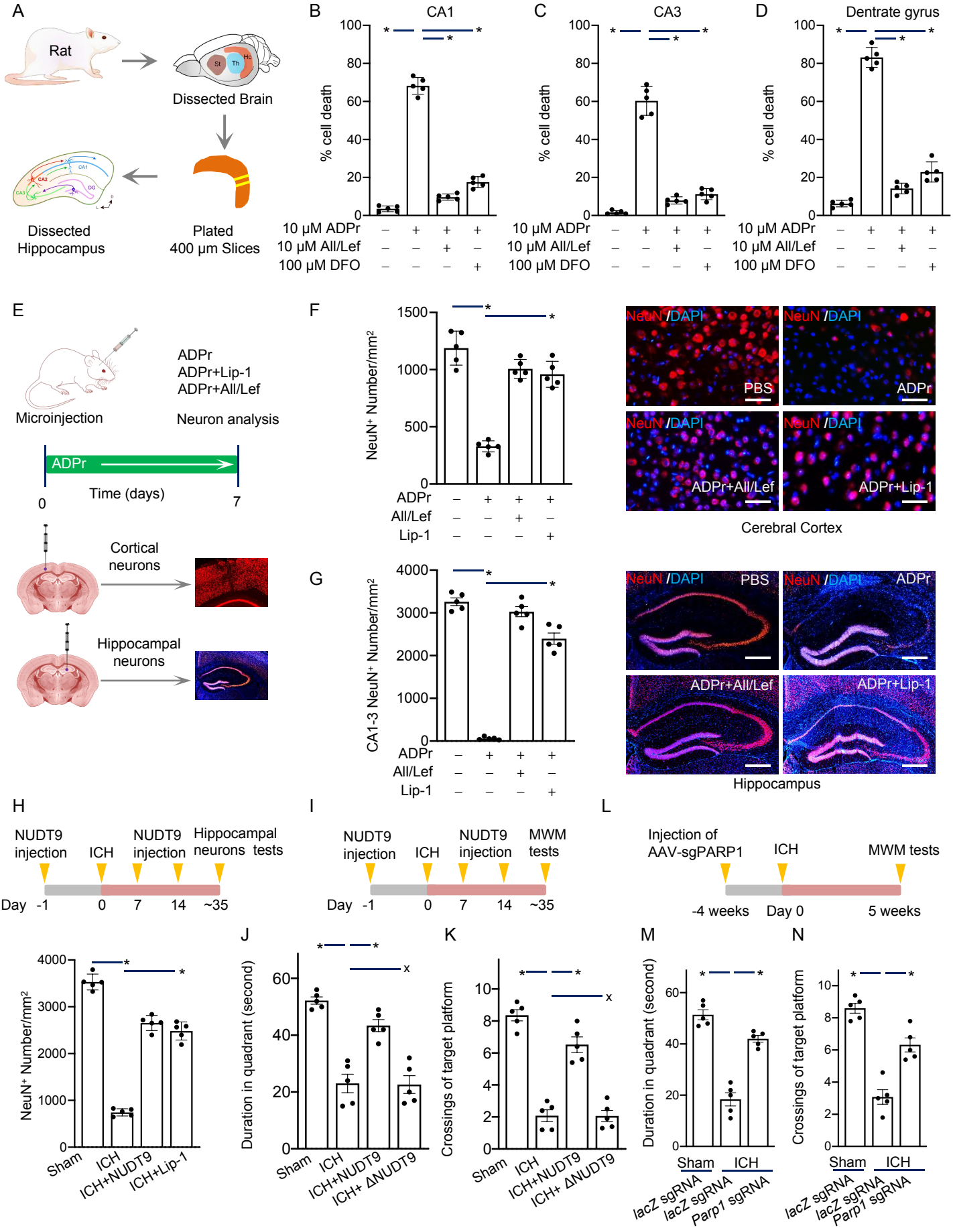
A
Rat
Dissected Brain
Dissected Hippocampus
Plated 400 μm Slices
B
CA1
% cell death
10 μM ADPr
10 μM All/Lef
100 μM DFO
C
CA3
D
Dentrate gyrus
E
Microinjection
ADPr
ADPr+Lip-1
ADPr+All/Lef
Neuron analysis
Time (days)
Cortical neurons
Hippocampal neurons
F
NeuN+ Number/mm2
ADPr
All/Lef
Lip-1
NeuN /DAPI
PBS
ADPr+All/Lef
ADPr+Lip-1
Cerebral Cortex
G
CA1-3 NeuN+ Number/mm2
Hippocampus
H
NUDT9 injection
ICH
Hippocampal neurons tests
Day -1 0 7 14 ~35
Sham
ICH+NUDT9
ICH+Lip-1
I
MWM tests
ICH+ ΔNUDT9
J
Duration in quadrant (second)
K
Crossings of target platform
L
Injection of AAV-sgPARP1
-4 weeks
Day 0
5 weeks
M
lacZ sgRNA
Parp1 sgRNA
N